UNIVERSITÉ DE MONTRÉAL

INTEGRATED OPTICS
MACH-ZEHNDER INTERFEROMETER SENSOR

Alireza MALEK-TABRIZI

DÉPARTEMENT DE GÉNIE PHYSIQUE

ÉCOLE POLYTECHNIQUE DE MONTRÉAL

MÉMOIRE PRÉSENTÉ EN VUE DE L'OBTENTION

DU DIPLÔME DE MAÎTRISE ÈS SCIENCES APPLIQUÉES

(GÉNIE PHYSIQUE)

AOÛT 1996

© Alireza MALEK-TABRIZI, 1996.

UNIVERSITÉ DE MONTRÉAL

ÉCOLE POLYTECHNIQUE

Ce mémoire intitulé:

INTEGRATED OPTICS
MACH-ZEHNDER INTERFEROMETER SENSOR

Présenté par: MALEK-TABRIZI, Alireza

en vue de l'obtention du diplôme de: Maîtrise ès sciences appliquées

a été dûment accepté par le jury d'examen constitué de:

M. MASUT, Remo, Ph.D., président

M. MARTINU, Ludvik, Ph.D., membre et directeur de recherche

M. NAJAFI, S. Iraj, Ph.D., membre et codirecteur de recherche

M. WERTHEIMER, Michel R., Ph.D., membre

à mes grand-parents Aghdas et Reza

REMERCIEMENTS

Je veux tout d'abord remercier sincèrement mon directeur et mon codirecteur de recherche, M. L. Martinu et M. S.I. Najafi. Ils m'ont donné tout le support scientifique et moral nécessaire pour compléter mon projet de recherche.

Je voudrais également remercier M. M.R. Wertheimer et M. R. Masut d'avoir accepté d'être membres du jury. J'espère qu'ils trouveront la lecture de ce mémoire intéressante.

Je me dois de remercier Mme J.E. Klemberg-Sapieha pour avoir éffectué les dépôts par plasma et M. D. Poitras pour m'avoir appris l'ABC de caracterisation optique des couches minces. J'apprécie également toutes les aides morales et scientifiques de mes amis aux groupes plasma et photonique.

Enfin, je voudrais remercier M. J. Chisham et M. A. Hamoutene pour m'avoir aidé à corriger le texte de ce mémoire, M. A. Tervonen pour ses conseils au niveau du design optique et M. Y. Lemire et M. G. Jalbert pour leur aide technique.

RÉSUMÉ

Le premier objectif de ce projet consiste à éffectuer le design, la fabrication et la caractérisation des guides d'onde optiques canaux par dépôt chimique en vapeur assisté par plasma (PECVD) d'oxynitrure de silicium et par échange ionique de potassium (PIE) dans le verre BK7. Ceci représente une fabrication initiale de guides planaires afin de trouver l'indice de réfraction et l'épaisseur (ou profondeur) des couches déposées ou diffusées. Ces données sont nécessaires pour le design des guides canaux monomodes qui sont ensuite fabriqués et caractérisés.

L'objectif principal de ce projet est de proposer le design, et de fabriquer et caractériser un capteur Mach-Zehnder. Ce capteur est un interferomètre sensible aux variations de l'indice de réfraction dans la gaine. Ces variations peuvent être créées par une perturbation externe comme des changements de température, de pression ou de la composition chimique de la gaine. Autrement dit, la grandeur mesurée par le capteur peut être toute cause impliquant une variation de l'indice de réfraction de la gaine. Le design et l'étude paramétrique du capteur ont été faits par la méthode de la propagation de

faisceau par différence finie (FD-BPM). Le fonctionnement du dispositif Mach-Zehnder a été démontré à l'aide de solutions de sucre dans l'eau à des concentrations différentes comme un matériau modèle. À chaque étape, le capteur a été couvert par une goute de la solution et le signal à la sortie a été enregistré. En conclusion, nous avons comparé de différents designs du capteur et leurs sensibilités, en particulier, du capteur Mach-Zehnder symétrique et non symétrique.

ABSTRACT

The first objective of this project was to design, fabricate and characterize straight channel optical waveguides prepared by plasma enhanced chemical vapor deposition (PECVD) of silicon oxynitride and by potassium ion exchange (PIE) in BK7 glass. This involved initial fabrication of slab waveguides by the two methods, and determination of the refractive index and thickness (or depth) of the deposited or diffused films. Having obtained these data, the next step was to design single-mode waveguides, which were then fabricated and characterized.

The main objective was to design, fabricate and characterize a nonsymmetric Mach-Zehnder interferometer sensor. This device is a refractive index sensor that is sensitive to the variations in the refractive index of the cladding layer. These variations can be created by an external perturbation such as change of temperature, pressure or chemical composition of the cladding layer. The design and a parametric study of the interferometer was performed using the finite difference beam propagation method (FD-BPM). The sensor testing and characterization was carried out using a solution of

different concentrations of sugar in water as a model analyte material. During the measurements, the sensor was covered by a drop of the solution and the output was recorded. Finally, the sensitivities of the symmetric and non-symmetric Mach-Zehnder interferometers were evaluated and compared.

CONDENSÉ EN FRANÇAIS

Le progrès rapide dans le domaine de l'optique intégrée depuis les années soixante-dix est dû en partie à la découverte de fibres optiques en verre à faibles pertes.

Les capteurs optiques sont des dispositifs utilisant l'onde électromagnétique pour détecter une perturbation dans un milieu donné. Cette perturbation peut être une variation de température, de pression, de déplacement mécanique ou simplement une variation de la concentration d'une solution.

Les qualités principales de ces dispositifs sont l'immunité électromagnétique (EMI), le faible bruit (un rapport signal sur bruit élevé), le temps de réponse rapide et la grande sensibilité. Le coût d'un capteur optique reste bien supérieur à celui des capteurs électriques et mécaniques. Ceci constitue la cause principale de la faible exploitation de ces dispositifs par l'industrie des capteurs.

Les capteurs à l'onde évanescente sont préférables aux autres capteurs car les pertes par couplage sont minimisées. Ils sont divisés en deux types: le capteur à absorption et le capteur interférométrique. Dans le premier cas (capteur à absorption), la perturbation affecte la partie imaginaire de l'indice de réfraction de la gaine dans le capteur à guide d'onde. On observe alors une modulation d'amplitude à la sortie du capteur.

L'inconvénient principal de ces capteurs réside dans le fait que les grandeurs à mesurer ont pour la plupart leur bande d'absorption dans l'ultraviolet alors que les diodes lasers servant de source émettent dans le visible ou le proche infrarouge. Dans le second cas (capteur interférométrique), la perturbation affecte principalement la partie réelle de l'indice de réfraction de la gaine. On observe alors une modulation de phase à la sortie. Ces capteurs ont une sensibilité bien supérieure à celle des capteurs à absorption.

Jusqu'à présent, le capteur interférométrique "Mach-Zehnder" est le type de capteur interférométrique le plus facile à fabriquer. Sa fabrication ne nécessite pas de réseaux comme dans le cas du Fabry-Pérot.

Dans le cadre de ce projet, on a d'abord fabriqué et caractérisé des guides d'ondes optiques par le dépôt dans un plasma à basse pression et à échange ionique. La variation de l'indice de réfraction des guides d'ondes canaux à échange ionique est de 0.0081 pour le mode TE et 0.0110 pour le mode TM. Cette variation est identique à celle des guides d'ondes planaires à échange ionique. Mais leur profondeur de diffusion est inférieure à celle des guides d'ondes planaires. Cette profondeur diminue avec la diminution de la largeur du masque. La courbe de dispersion de l'indice de réfraction pour les couches déposées par plasma a été déterminée par la méthode de réflexion simulée. Les perte par propagation pour les guides d'ondes déposés par plasma à température ambiante étaient de 4 à 6 dB/cm pour différents échantillons.

On a ensuite mené une étude paramétrique par simulation de différents types d'interféromètre Mach-Zehnder en utilisant la méthode FD-BPM (la méthode de la propagation du faisceau par différences finies). Cette étude montre clairement que les capteurs Mach-Zehnder symétriques ont une sensibilité meilleure que celle des capteurs Mach-Zehnder non-symétriques pour longueurs de dispositif comparables. L'élargissement de l'ouverture dans le cas des capteurs symétriques et l'augmentation de

la différence de parcours géométrique dans le cas des capteurs non-symétriques améliorent la sensibilité du capteur. Les capteurs à guides rubans dans la région active ont une sensibilité plus élevée que les capteurs à guides d'ondes enterrés. Ceci peut être expliqué par une région d'interaction plus large pour les capteurs à guides rubans dans la zone active. Les interférométres Mach-Zehnder avec des coupleurs à la place des jonctions Y présentent les mêmes caractéristiques que ceux avec des jonction Y.

Du point de vue de la fabrication, le Mach-Zehnder non-symétrique est plus facile à fabriquer que le Mach-Zehnder symétrique car il nécessite un seul niveau de masque en photolithographie.

En utilisant les caractéristiques du guide d'onde trouvées pour échange ionique dans les substrat BK7, on a fait le design et la fabrication d'un interférométre Mach-Zehnder non-symétrique.

Pour vérifier la fonction du capteur on a utilisé un laser He-Ne polarisé comme source. Le capteur a été caracterisé à l'aide d'une solution de sucre de concentration

connue. Le signal à la sortie a été enregistrée à l'aide d'un photodétecteur en silicium. Cette opération a été répétée pour différentes concentrations de la solution. Les données enregistrées étaient en très bon accord avec celles trouvées par simulation FD-BPM pour le même dispositif.

TABLE OF CONTENTS

PAGE

DÉDICACE....iv

REMERCIEMENTS....v

RÉSUMÉ....vi

ABSTRACT....viii

CONDENSÉ EN FRANÇAIS....x

TABLE OF CONTENTS....xv

LIST OF FIGURES....xviii

LIST OF TABLES....xxv

PREVIEW....xxvii

CHAPTER 1- INTRODUCTION....1

CHAPTER 2- THEORETICAL BACKGROUND....6

2.1 OPTICAL WAVEGUIDES....6

2.2 STEP INDEX 2-D WAVEGUIDES....8

2.3 GRADED INDEX 2-D WAVEGUIDES....12

2.4 WKB METHOD....12

2.5 3-D WAVEGUIDES....13

2.6 EFFECTIVE INDEX METHOD (EIM)....14

PAGE

2.7 FINITE DIFFERENCE METHOD (FDM).....16

2.8 BUFFER LAYER.....16

2.9 BENT WAVEGUIDE.....16

2.10 BEAM PROPAGATION METHOD (BPM).....18

CHAPTER 3- WAVEGUIDE FABRICATION METHODS.....19

3.1 ION EXCHANGE.....19

3.1.1 THERMAL ION EXCHANGE.....20

3.1.2 REFRACTIVE INDEX INCREASE FROM ION EXCHANGE.....21

3.1.3 FABRICATION OF ION EXCHANGE WAVEGUIDES.....23

3.2 PLASMA ENHANCED CHEMICAL VAPOUR DEPOSITION.....26

3.2.1 PROCESSES IN LOW PRESSURE PLASMA.....26

3.2.2 OPTIMIZATION OF DEPOSITION CONDITIONS.....27

3.2.3 RIDGE WAVEGUIDE FABRICATION USING PECVD.....32

3.3 WAVEGUIDE CHARACTERIZATION.....32

3.3.1 PRISM COUPLING METHOD.....34

3.3.2 GRATING METHOD.....35

3.3.3 TRANSMISSION AND REFLECTION METHOD.....37

3.3.4 LOSS MEASUREMENT.....39

3.3.4.1 END-COUPLING METHOD.....39

3.3.4.2 SCATTERED LIGHT MEASUREMENT METHOD.....40

PAGE

CHAPTER 4- WAVEGUIDE FABRICATION AND CHARACTERIZATION: RESULTS.....42

4.1 K^+- EXCHANGE WAVEGUIDES.....42

4.2 PECVD SiO_xN_y WAVEGUIDES.....47

CHAPTER 5- COMPARISON OF DIFFERENT MACH-ZEHNDER INTERFEROMETER SENSORS.....53

5.1 TWO-BEAM INTERFEROMETRY.....53

5.2 DEVICE STRUCTURE.....54

5.3 DEVICE OPERATION.....57

5.4 DISCUSSION.....59

CHAPTER 6- NONSYMMETRIC MACH-ZEHNDER INTERFEROMETER SENSOR.....69

6.1 DESIGN.....69

6.2 TESTING.....71

CHAPTER 7- CONCLUSIONS.....73

REFERENCES.....75

LIST OF FIGURES

PAGE

Figure 1.1 3

The principle of evanescent-wave sensors.

Figure 1.2 3

Schematic illustration of a Mach-Zehnder interferometer: a)symmetric, b)nonsymmetric.

Figure 2.1 7

Schematic illustration of a 2-D optical waveguide.

Figure 2.2 11

Normalized dispersion curves for the planar step-index waveguides for different asymmetry factors, a: (a = 0 ——), (a = 1– – – – ·), (a = 10– · – ·), (a = ∞ · · · · ·).

Figure 2.3 15

Analytical model for the effective index method.

Figure 2.4 17

Schematic illustration of a bent waveguide.

PAGE

Figure 3.1 25

Steps in the fabrication of ion-exchanged waveguides.

Figure 3.2 30

Schematic illustration of a dual-mode microwave/radiofrequency (MW/RF) plasma reactor (From Martinu, L, 1996).

Figure 3.3 31

Refractive index (at λ~600 nm) of SiO_xN_y films deposited in a MW/RF plasma as a function of N_2O /(N_2O + NH_3) gas flow ratio (•) (after Poitras et al.). For comparison, the results from a pure MW discharge using T_s=280°C (o) are shown (after Blain et al., 1989).

Figure 3.4 33

Fabrication steps of ridge waveguide prepared by PECVD.

Figure 3.5 36

Prism coupling for measuring effective indices of modes.

PAGE

Figure 3.6.....36

Grating method for measuring effective indices of modes.

Figure 3.7.....38

Typical refractive index dispersion curves of low pressure plasma-deposited SiO_2, SiO_xN_y and $SiN_{1.3}$ films deposited in MW/RF plasma.

Figure 3.8.....41

Loss measurement using fiber end-coupling.

Figure 3.9.....41

Loss measurement by scattered light.

Figure 4.1.....49

Refractive index dispersion found for thermally grown SiO_2.

Figure 4.2.....49

Refractive index dispersion found for SiO_xN_y deposited by PECVD.

PAGE

Figure 4.3 50

SEM micrographs of ridge waveguides fabricated from the same PECVD SiO_xN_y film using masks with different opennings: W = 2 μm (the first two), and W = 6 μm (the last).

Figure 4.4 51

Scattered light measurement result in μW for PECVD SiO_xN_y ridge waveguide deposited at ambient substrate temperature and using W ≒ 6 μm as in Figure 4.3. The solid curve is an exponential fit of the experimental points. Propagation loss ≅ 5.0±0.1 dB/cm.

Figure 4.5 52

Scattered light measurement result in μW for PECVD SiO_xN_y ridge waveguide deposited at ambient substrate temperature and using W = 2 μm as in Figure 4.3. The solid curve is an exponential fit of the experimental points. Propagation loss ≅ 7.6±0.1 dB/cm.

Figure 5.1 56

Schematic illustration of different Mach-Zehnder interferometers and their active region refractive index profile (Malek-Tabrizi et al., 1996).

PAGE

Figure 5.2.a.....61

FD-BPM simulation of power in the Mach-Zehnder interferometer MZ1 (see Figure 5.1) with ΔΦ=180° (from Malek-Tabrizi et al., 1996).

Figure 5.2.b.....62

FD-BPM simulation of power in the Mach-Zehnder interferometer MZ1 (see Figure 5.1) ΔΦ=0° (from Malek-Tabrizi et al., 1996).

Figure 5.2.c.....63

FD-BPM simulation of power in the Mach-Zehnder interferometer MZ4 (see Figure 5.1) with ΔΦ=180° (from Malek-Tabrizi et al., 1996).

Figure 5.2.d.....64

FD-BPM simulation of power in the Mach-Zehnder interferometer MZ4 (see Figure 5.1) with ΔΦ=0° (from Malek-Tabrizi et al., 1996).

Figure 5.3.....65

Mach-Zehnder interferometer sensor output intensity as a function of superstrate refractive index for symmetric MZ1 and nonsymmetric MZ2 interferometers (see Figure

PAGE

5.1). l = window opening length for symmetric interferometer, Δl = path-length difference for nonsymmetric interferometer, L = device length (from Malek-Tabrizi et al., 1996).

Figure 5.4.....66

Mach-Zehnder interferometer sensor output intensity as a function of the superstrate refractive index for nonsymmetric MZ2 interferometer (see figure 5.1). Δl = path-length difference, L = device length (from Malek-Tabrizi et al., 1996).

Figure 5.5.....67

Mach-Zehnder interferometer sensor output intensity as a function of superstrate refractive index for ridge waveguide MZ1 and buried waveguide MZ3 symmetric interferometers (see figure 5.1). l = window opening length, L = device length (from Malek-Tabrizi et al., 1996).

Figure 5.6.....68

Mach-Zehnder interferometer output intensity as a function of the superstrate refractive index for symmetric MZ4 interferometer (see figure 5.1). l = window opening length, L = device length (from Malek-Tabrizi et al., 1996).

PAGE

Figure 6.1 70

Mask layout and parameters for the Mach-Zehnder sensors.

Figure 6.2 70

Mode profile of the device calculated for potassium ion-exchange for 2 hours.

Figure 6.3 71

Setup for testing the prototype nonsymmetric MZI.

Figure 6.4 72

Refractive index of the analyte solution as a function of its concentration at T=20°C and λ=0.633 μm.

Figure 6.5 72

Normalized output power of a prototype nonsymmetric MZI vs. cladding refractive index: experimental data (■) compared with the FD-BPM simulation (solid line).

LIST OF TABLES

PAGE

Table 4.1 44

Prism coupling results (effective index, N_m) for K^+-exchanged channel waveguides (t = 25 hours) with different mask openings (W) and for different modes of propagation (m) at the HeNe laser (λ = 0.6328 μm) wavelength (TE-polarization) and n_s (λ = 0.6328 μm) = 1.5151.

Table 4.2 45

Prism coupling results (effective index, N_m) for K^+-exchanged channel waveguides (t = 25 hours) with different mask openings (W) and for different modes of propagation (m) at the HeNe laser (λ = 0.6328 μm) wavelength. (TM-polarization) and n_s (λ = 0.6328 μm) = 1.5151.

Table 4.3 45

Prism coupling results (effective index, N_m) for K^+-exchanged channel waveguides (t = 25 hours) with different mask openings (W) and for the fundamental mode (m_o) at the Nd:YAG laser (λ = 1.0639 μm) wavelength (TE-polarization) and n_s (λ = 1.0639 μm) = 1.5065.

PAGE

Table 4.4.....46

Prism coupling results (effective index, N_m) for K^+-exchanged channel waveguides (t = 25 hours) with different mask openings (W) and for the fundamental mode (m_o) at the Nd:YAG laser (λ = 1.0639 μm) wavelength (TM-polarization) and n_s (λ = 1.0639 μm) = 1.5065.

Table 4.5.....46

Prism coupling results (effective index, N_m) for K^+-exchanged slab waveguides (t = 25 hours) for different modes of propagation (m) at the HeNe laser (λ = 0.6328 μm) wavelength and n_s (λ = 0.6328 μm) = 1.5151.

Table 4.6.....47

Thickness, d, refractive index difference, Δn, and apparent diffusion coefficient, D, values obtained for the K^+-exchanged channel waveguides (t = 25 hours, TM-polarization).

PREVIEW

The first chapter of this thesis gives an introduction to the concept of integrated optics sensors and it concludes with a literature review of Mach-Zehnder interferometer sensors. The second chapter is a theoretical reminder of the guided wave theory, and it presents the concepts used in this work. The third chapter explains the fabrication and the characterization methods exploited in this work. The fourth chapter presents the experimental results obtained from waveguide fabrication and characterization. The fifth chapter is a comparative study of different types of Mach-Zehnder sensor; the simulations in this chapter are performed by finite difference beam propagation method (FD-BPM)[⊠]. The sixth chapter explains the design and the fabrication of a prototype Mach-Zehnder chemical sensor; it presents a characteristic "calibration" curve obtained from the sensor testing.

This work has contributed to the following paper which was presented at the SPIE's Photonic West '96 symposium:

"Glass Integrated Optics Symmetric and Non-Symmetric Mach-Zehnder Interferometer Sensors", A. MALEK-TABRIZI, S.I. NAJAFI and L. MARTINU, Conf. on Integrated Optics and Optical Fibers Devices, San Jose, Feb. 1996, Proc. SPIE 2695.

[⊠] The OPTONEX software for design and simulation of integrated optical circuits, Espoo, Finland.

The author of this thesis has also actively contributed to the following works during the period of his master project:

"UV-Light Imprinted Sol-Gel Silica Glass Low-Loss Waveguides for Use at 1.55 μm", P. COUDRAY, J. CHISHAM, M.P. ANDREWS, A. MALEK-TABRIZI, C.Y. LI, S.I. NAJAFI, submitted to the SPIE J. of Optical Engineering.

"Ultraviolet Light Imprinted Sol-Gel Silica Glass Devices on Silicon", P. COUDRAY, J. CHISHAM, A. MALEK-TABRIZI, C.Y. LI, M.P. ANDREWS, N. PEYGHAMBARIAN and S.I. NAJAFI, Submitted to the J. of Optics Communication.

"UV-Imprinted Sol-Gel Silica Glass Channel Waveguides on Silicon", S.I.NAJAFI, C.Y.LI, J. CHISHAM, M. ANDREWS, A. MALEK-TABRIZI and N. PEYGHAMBARIAN, SPIE's Conf. on Integrated Optics and Optical Fibers Devices, San Jose, Feb. 1996, Proc. SPIE 2695 .

"UV-Light Imprinted Y-Splitter in Sol-Gel Silica Glass", P.COUDRAY, C.Y.LI, A. MALEK-TABRIZI, J. CHISHAM, M.ANDREWS, S.I.NAJAFI, and N. PEYGHAMBARIAN, SPIE's Conf. on Integrated Optics and Optical Fibers Devices, San Jose, Feb. 1996, Proc. SPIE 2695.

"UV-Light Imprinted and Embossed Gratings in Sol-Gel Silica Glass", J. CHISHAM, S.I.NAJAFI, M. ANDREWS, A. MALEK-TABRIZI, SPIE's Conf. on Integrated Optics and Optical Fibers Devices, San Jose, Feb. 1996, Proc. SPIE 2695.

"Ridge and Buried Sol-Gel Waveguides on Silicon", A. FARDAD, A. MALEK-TABRIZI, M.P. ANDREWS and S.I. NAJAFI, Submitted to the J. of Applied Optics.

CHAPTER 1

INTRODUCTION

Research in Integrated Optics (IO) accelerated in 1970's mainly due to the discovery of low-loss silica optical fibers. It created a need for greater bandwidth in telecommunications and better sensors. These sensors, that could form smart structures, are specified by their very high sensitivity and immunity to electromagnetic interference (Udd, 1991).

Optical Integrated Circuits (OIC) are distinguished by their special features. Development of thin film technology and photolithography has made their mass production possible, and has also reduced the amount of material needed. OIC's are very compact and light. Optical power density in single-mode waveguides is much higher than optical beam in free space, and this enables the utilization of nonlinear effects in waveguide materials. Finally, an optical integrated circuit has no assembly problems since several discrete elements can been integrated on a single substrate (H. Nishihara et al.,1989).

Optical sensors are devices that use electromagnetic waves in sensing a perturbation in their surrounding media. This perturbation can be a change in temperature, in pressure, a displacement or simply a change in concentration of the surrounding environment.

The immunity to electromagnetic interference (EMI), low noise, small delay and high sensitivity are main virtues that make these devices attractive. Nevertheless, there is only a very small part of the sensor industry which is exploiting optical sensors. This is brought about by higher prices of these "hi-tech" devices in comparison with their electrical or mechanical counterparts. Therefore, new techniques for material synthesis and device fabrication are being investigated which will allow large volume, low-cost production.

Evanescent-wave sensors are preferred to others because light does not leave their waveguides or optical fibers. Therefore, the coupling losses are minimized. Such sensors can be divided into two groups: absorptive and interferometric (Figure 1.1).

In absorptive sensors, the perturbation affects the imaginary part of the refractive index of the cladding on the waveguide sensor, so we can observe intensity modulation in the output of the sensor. This type of sensor can be thought of as the evanescent field analogy of spectroscopy. The main drawback is the fact that most of the analytes have their absorption band in the ultraviolet region while the diode laser sources usually emit in the visible or near infrared regions.

In interferometric sensors, the perturbation affects mainly the real part of the refractive index of the cladding, so we can observe intensity modulation in the output. Interferometric sensors are far more sensitive than absorptive sensors because they are based on phase modulation, and the interferometer converts this phase modulation into intensity modulation in its output. The Mach-Zehnder interferometer (MZI) sensor, which is illustrated in Figure 1.2 and which will be described in more detail in Chapter 5, is the

simplest kind of interferometric sensor to fabricate; for instance, its fabrication does not require gratings as in the case of a Fabry-Perot interferometer.

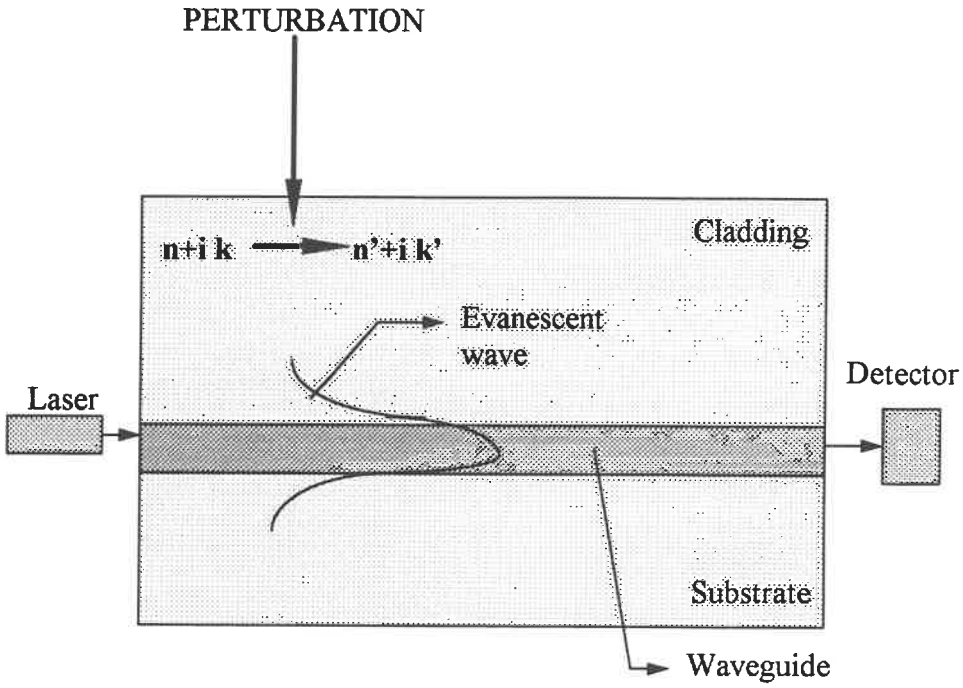

Figure 1.1. The principle of evanescent-wave sensors.

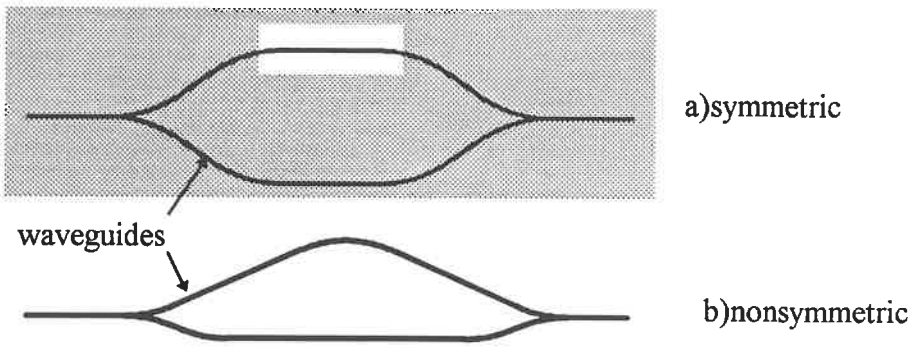

Figure 1.2. Schematic illustration of a Mach-Zehnder interferometer: a)symmetric, b)nonsymmetric.

The first IO sensor, used as a thermometer, was studied by Johnson et al., 1982. It was a non-symmetric MZI made in $LiNbO_3$. Its optical transmission varies sinusoidally with temperature with a period inversely proportional to the path length difference between the two arms. This device has a projected range and resolution of >700°C and 2×10^{-3} °C, respectively.

An optical pressure sensor consisting of a MZI and a thin membrane anisotropically etched into the silicon substrate underneath the measuring arm of the interferometer was successfully fabricated (Wagner et al., 1993). Pressure sensors are made on silicon substrate because of the possibility of monolithic integration of electronic as well as optical circuits, and of microstructural features, such as grooves, holes, diaphragms, and cantilevers, which can be formed with high precision on the silicon substrate using anisotropic etching (Ohkawa et al., 1989).

Silicon oxynitride (SiO_xN_y) thin films can be deposited by thermal oxidation and by Low-Pressure Chemical Vapour Deposition (LPCVD), and they may be patterned by means of lithography and plasma etching. The refractive index of the silicon oxynitride waveguide layer, sandwiched between two silicon dioxide layers, is adjustable. The relation of the propagation properties to elongation and temperature has been studied to determine if IO interferometer structures may be used as sensors (Fischer et al., 1992).

A MZI was proposed as a basic optical device for a new hydrogen sensor. The sensitivity to hydrogen is obtained through refractive index changes induced by absorption or desorption of hydrogen in a thin film of palladium deposited on one of the

two branches of the interferometer (Bearzotti et al., 1992). A MZI was also proposed as a displacement sensor (Helleso et al., 1995).

Fabricius et al., 1992, demonstrated a sensor system for measuring gaseous compounds using a MZI. One of the surface waveguide arms of the IO device is covered with a polysiloxane layer, sensitive to organic solvents. The refractive index of the polymer layer changes according to the partial pressure of the vapor of such solvents.

Helmers et al., 1996, fabricated an evanescent-wave MZI sensor for the detection of heptane vapor. They reported an angular precision of better than 10^{-3} for the phase shift which corresponds to superstrate index change inferior to 10^{-6}.

As already mentioned above, further research is needed to identify new materials, techniques and design to fabricate IO devices at a lower cost and in larger volumes. Based on that, the objectives of this thesis are the following:

(1) To study the Plasma Enhanced Chemical Vapour Deposition (PECVD) and Potassium Ion Exchange (PEI) as two promising methods for the fabrication of waveguides. This work involves the fabrication and characterization of straight waveguides by the two methods.

(2) To study and compare different designs of Mach-Zehnder interferometer chemical sensors.

(3) To design, fabricate and characterize a prototype nonsymmetric Mach-Zehnder interferometer chemical sensor.

CHAPTER 2

THEORETICAL BACKGROUND

This chapter describes the theoretical techniques that were exploited in the design and material characterization of the MZI sensors. The limitations and strengths of these techniques are explained in more detail by Nishihara et al., (1989) and Najafi, (1992).

2.1. OPTICAL WAVEGUIDES

If a thin film is deposited on a transparent dielectric substrate with a refractive index lower than that of the film, an optical waveguide will be formed. The light cannot be guided unless the refractive index of the film (n_f) is greater than the refractive indices of the substrate (n_s) and of the cladding or the superstrate (n_c).

In a 2-D (slab) waveguide, light is confined only in the x-direction, but in a 3-D (channel) waveguide, light is confined both in the x- and y-directions. In a step index waveguide, the refractive index changes abruptly along the depth, but in a graded index waveguide, the refractive index changes gradually along the depth (Figure 2.1).

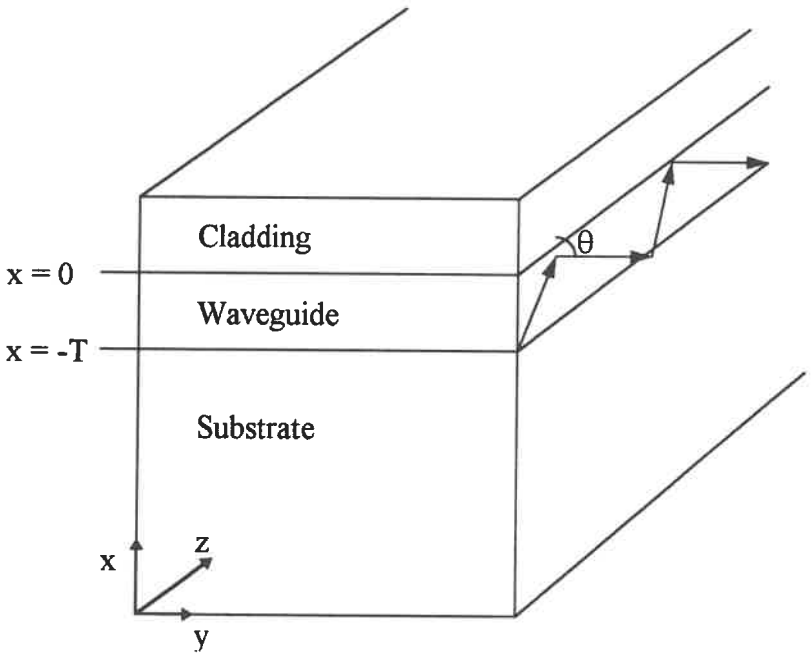

Figure 2.1. Schematic illustration of a 2-D optical waveguide.

2.2. STEP INDEX 2-D WAVEGUIDES

As stated earlier, light can propagate if the refractive index of the film is greater than the refractive indices of the substrate and the cladding ($n_f > n_c$, n_s). The relationship between the angle of incidence, θ (see Figure 2.1), and the propagation constants in the x and z directions (k_x, k_z) are:

$$k_x = k_o n_f \cos(\theta) \tag{2.1}$$

$$k_z = k_o n_f \sin(\theta) = \beta \tag{2.2}$$

where $k_o=(2\pi)/\lambda$, and β is the propagation constant in a lossless waveguide. The effective index (N_{eff}) of the mode can be defined as β/k_o. N_{eff} can be equally described as the refractive index that a guided mode sees along the waveguide. We know that the guided mode can be supported only for $\sin^{-1}(n_s/n_f) < \theta < 90°$, so for a propagated mode, $n_s<N_{eff}<n_f$.

The wave propagation in lossless dielectric media can be described by Maxwell's equations:

$$\nabla x E = -\mu_o \frac{\partial H}{\partial t} \tag{2.3}$$

$$\nabla x H = \varepsilon_o n^2 \frac{\partial E}{\partial t} \tag{2.4}$$

where ε_o and μ_o are the dielectric permittivity and magnetic permeability of free space, respectively, and n is the refractive index of the medium. If we solve the above coupled equations in a Cartesian coordinate system we will obtain:

$$E = E(x,y).e^{j(\omega t-\beta z)} \tag{2.5}$$

$$H = H(x,y).e^{j(\omega t-\beta z)} \tag{2.6}$$

where E and H denote complex electric and magnetic field vectors, respectively, the angular frequency $\omega=2\pi c/\lambda$, and c is the light velocity in free space ($c = \frac{1}{\sqrt{\varepsilon_o \mu_o}}$). In slab 2-D waveguides light is confined only in the x direction. Equations (2.3) and (2.4) yield two different modes with mutually orthogonal polarization states (TE and TM). TE consists of E_y, H_x, and H_z; TM consists of E_x, H_y and E_z.

The field solutions for the TE mode are:

$$E_y = E_c e^{(-\gamma_c x)} \quad \text{, in the cladding, } x > 0 \tag{2.7}$$

$$E_y = E_f \cos(k_x x + \phi_c) \quad \text{, in the film, } -T < x < 0 \tag{2.8}$$

$$E_y = E_s e^{(\gamma_s (x+T))} \quad \text{, in the substrate, } x < -T \tag{2.9}$$

where $\gamma_c=k_o(N_{eff}^2-n_c^2)^{1/2}$, $k_x=k_o(n_f^2-N_{eff}^2)^{1/2}$, $\gamma_s=k_o(N_{eff}^2-n_s^2)^{1/2}$, $\phi_c = k_x T/2$ and T is the waveguide thickness. Using the boundary conditions and eliminating the arbitrary coefficient, one obtains the eigenvalue equation for the TE mode (Nishihara et al., 1989):

$$k_x T = (m+1)\pi - \tan^{-1}\left(\frac{k_x}{\gamma_s}\right) - \tan^{-1}\left(\frac{k_x}{\gamma_c}\right) \tag{2.10}$$

where m = 0, 1, 2, ... is the mode number. Introducing the following normalization parameters can normalize the eigenvalue equation:

Normalized frequency: $$V = k_o T\sqrt{n_f^2 - n_s^2} \tag{2.11}$$

Normalized index: $$b_E = \frac{N_{eff}^2 - n_s^2}{n_f^2 - n_s^2} \tag{2.12}$$

Asymmetry factor: $$a_E = \frac{n_s^2 - n_c^2}{n_f^2 - n_s^2} \tag{2.13}$$

This will result in the normalized dispersion equation and the normalized dispersion curves (Figure 2.2):

$$V\sqrt{1-b_E} = (m+1)\pi - \tan^{-1}\sqrt{\frac{1-b_E}{b_E}} - \tan^{-1}\sqrt{\frac{1-b_E}{b_E+a_E}} \tag{2.14}$$

This equation is useful for designing slab step-index waveguides for TE propagation.

One can perform the same analysis for the TM modes to obtain the TM mode eigenvalue equation (Nishihara et al., 1989):

$$k_x T = (m+1)\pi - \tan^{-1}(\frac{n_s}{n_f})^2(\frac{k_x}{\gamma_s}) - \tan^{-1}(\frac{n_c}{n_f})^2(\frac{k_x}{\gamma_c}) \tag{2.15}$$

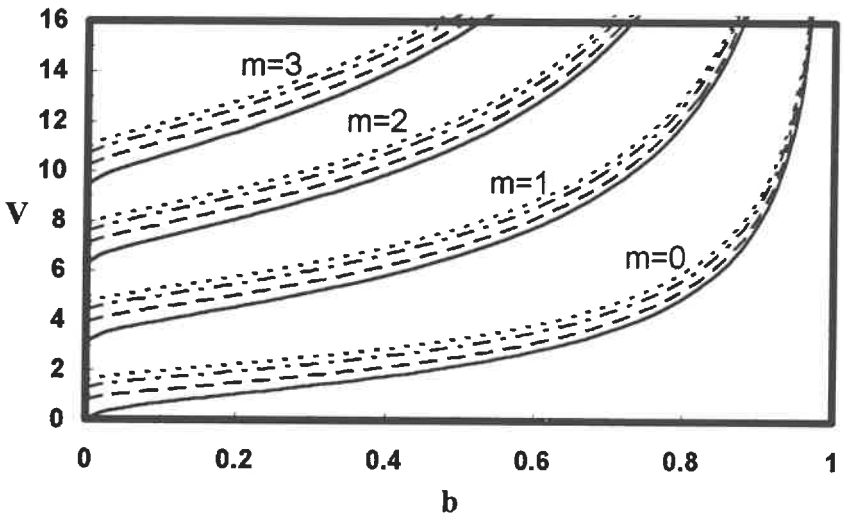

Figure 2.2. Normalized dispersion curves for the planar step-index waveguides for different asymmetry factors, a: (a = 0 ———), (a = 1 – – – –), (a = 10– · – · ·), (a = ∞ · · · · · · ·).

2.3. GRADED INDEX 2-D WAVEGUIDE

Graded index optical waveguides can be fabricated by metal-diffusion and ion-exchange techniques in glass (Tervonen, 1990). The index distribution of a diffused waveguide can be written in the form (Najafi, 1992)

$$n(x) = n_s + \Delta n . f(x / d) \tag{2.16}$$

where n_s is the substrate index, Δn is the maximum difference between the refractive indices of the substrate and the guiding layer, d is the depth at which n(x) takes on 1/e of its maximum value and f(x/d) is a monotonically decreasing function that takes on values between 0 and 1, and it follows the experimentally determined index variation.

2.4. WKB METHOD

The WKB (Wentzel-Kramers-Brillouin) method is used to solve the wave equation (Nishihara et al., 1989). It can also be adapted to find Δn and d in a graded index planar waveguide given the effective index of the modes.

The guided mode has always a total phase shift equal to a multiple of 2π for a round trip:

$$2k_0 \int_0^{x_t} \left[n^2(x) - N_m{}^2 \right]^{1/2} dx - \phi_c - \phi_s = 2m\pi \tag{2.17}$$

where m=0,1,2,... is the mode number, x_t is both the turning point for the mode and the solution of the equation $n(x_t)=N_m$. N_m is the effective index for the mth mode. ϕ_c and ϕ_s are

the phase shifts due to the total internal reflection at the points x=0 and $x=x_t$ (Najafi, 1992):

$$\phi_c = 2\arctan\left\{p\left[\left(\beta^2 - k_o^2 n_c^2\right)/\left(k_o^2 n_f^2 - \beta^2\right)\right]^{1/2}\right\} \tag{2.18}$$

$$\phi_s = \pi/2 \tag{2.19}$$

where p = 1 for TE-polarization, $p = (n_f/n_c)^2$ for TM-polarization and $n_f = n_s + \Delta n$.

The WKB method calculates the left hand side in the equation 2.17, which is a function of Δn and d. When Δn and d are changed so much that they satisfy the equation 2.17 then one obtains optimum values for these two parameters. We should notice that the integration limit (x_t) itself is a function of Δn and d, so x_t should be recalculated in each iteration.

2.5. 3-D WAVEGUIDES

IO devices such as switches, sensors and modulators require light confinement in lateral y-direction in addition to the depth x-direction. The reason is that in slab waveguides the propagated light usually diverges after few millimeters. 3-D optical waveguides (channel waveguides) can be fabricated in a variety of ways such as ion-exchange and plasma dry etching. There are several methods for the analysis of channel waveguides, such as effective index method and finite difference method.

2.6. EFFECTIVE INDEX METHOD (EIM)

EIM is an approximate analysis for determining effective index and mode profile of the guided modes in waveguides (Najafi, 1992). Figure 2.3 shows an example of a step index buried waveguide. This method is useful for cases where Δn (the difference between the refractive indices of the substrate and of the guiding layer) is very small. In this method the buried 3-D waveguide is divided into 2-D waveguide I with light confinement in the x direction (Figure 2.3b), and 2-D waveguide II with light confinement in the y direction (Figure 2.3c). The modes have main field components E_x and H_y in 2-D waveguide I. The eigenvalue equation (2.15) yields the effective index, N_I, of the TM mode with field components E_x, H_y, and E_z. Alternatively, the corresponding value of the normalized guide index, b_I, can be obtained graphically using the dispersion curves in Figure 2.2. Therefore,

$$N_I = \sqrt{n_s^2 + b_I(n_f^2 - n_s^2)} \tag{2.20}$$

The slab waveguide II (Figure 2.3c) sees the effective index, N_I , as a refractive index of its guiding layer.

Waveguide II is polarized along the x direction and the guided mode is TE. Therefore, we can write its normalized dispersion equation as:

$$V_{II}\sqrt{1-b_{II}} = (m+1)\pi - 2\tan^{-1}\sqrt{\frac{1-b_{II}}{b_{II}}} \tag{2.21}$$

Using the dispersion curves (Figure 2.2) and setting $a_E = 0$ (such as in Figure 2.3c), we can find the effective refractive index graphically (Nishihara et al., 1989).

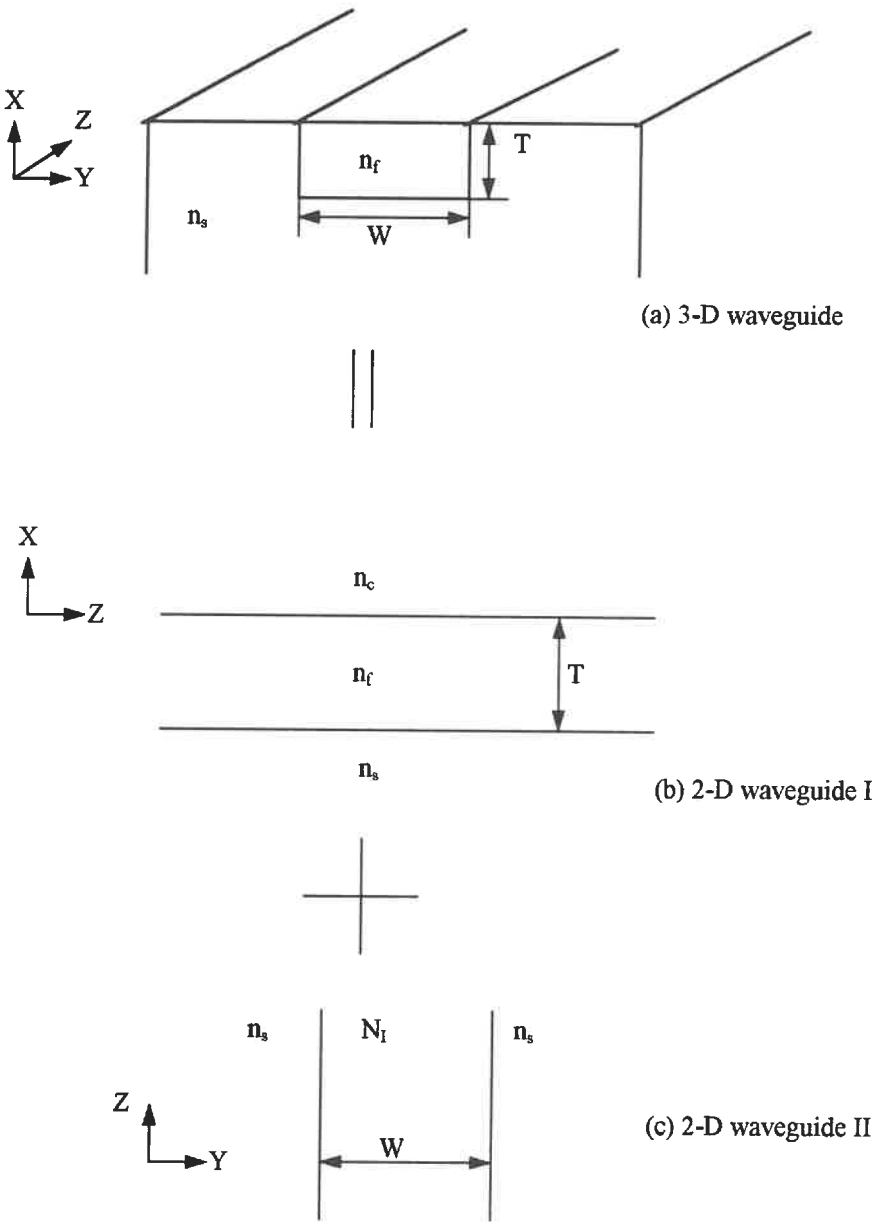

Figure 2.3. Analytical model for the effective index method.

2.7. FINITE DIFFERENCE METHOD (FDM)

FDM is an accurate method for finding the propagation constant and the mode profile in a 3-D waveguide (Najafi, 1992). When the concentration distribution of an ion-exchanged waveguide has been modeled by FDM and then transformed to the refractive index profile, this profile is given by discrete values of refractive index in points of a rectangular grid, which is explained in more detail in the section 3.1.2.. The wave equation or the variational forms derived from it can also be written in finite difference form for these grid points (Najafi, 1992).

2.8. BUFFER LAYER

Waveguides cannot be obtained by direct deposition of a thin film on Si because Si has a large refractive index and exhibits a large leakage loss. For this reason, a SiO_2 layer is grown as an *optical buffer layer* on the surface of silicon. To reduce the leakage loss to an acceptable value, the SiO_2 layer thickness must be chosen at a value sufficiently larger than the depth of the guided-wave penetration into this layer (usually 2 to 10 μm). The necessary SiO_2 thickness depends on the refractive index and on the thickness of the waveguide film as well as on the wavelength.

2.9. BENT WAVEGUIDE

Bent waveguides are necessary in optical integrated circuits to change the direction of the light. A smaller radius of curvature permits us to change the direction of

propagation in a shorter distance but it entails high radiation loss (see Figure 2.4). To maintain a guided mode with equiphase front on the radial plane (plane perpendicular to the propagation vector) the phase velocity of the guided mode may change in the radial direction on the wave front plane. As we move on the radial plane outwards the phase velocity of the guided mode gets larger because it moves longer distance in the same period of time. A critical radius r_c exists above which the guided mode's phase velocity is larger than the speed of light. Therefore, the part of the evanescent tail larger than r_c corresponds to the radiation loss due to the curvature (Nishihara et al., 1989).

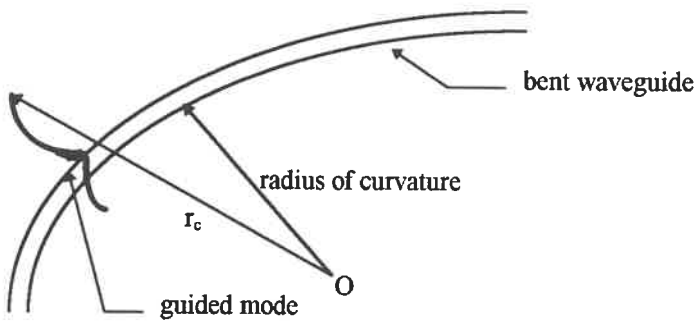

Figure 2.4. Schematic illustration of a bent waveguide.

2.10. BEAM PROPAGATION METHOD (BPM)

Once the index profile and the layout of the optical integrated circuit are known, one can use the BPM to simulate the light intensity propagation throughout the device (Najafi, 1992). This is a convenient technique for the design of optical integrated circuits because it gives us an evaluation of the device prior to actual fabrication.

Basically, using the distribution of electric field and mode profile at a position z, BPM calculates the distribution of electric field at a further position $z+\delta$. There are two types of BPM. The first type is based on fast Fourier transformation, and it is called FFT-BPM. The second type, based on finite difference method, is called FD-BPM (Pace et al., 1994).

The computational speed of FD-BPM is much greater than that of FFT-BPM. FD-BPM is more stable than FFT-BPM with respect to the propagation step size and number of grid points variation. For comparable accuracy, one needs smaller propagation step size in the FFT-BPM than in the FD-BPM (Chung et al., 1990).

CHAPTER 3

WAVEGUIDE FABRICATION METHODS

This chapter covers PIE and PECVD as two promising methods for fabrication of IO devices based on glass and silicon oxynitride. Different methods for characterization of straight waveguides are explained.

Many kinds of materials and processing techniques have been tested for optical waveguides formed by a layer with a slightly higher refractive index than for the substrate. The waveguides can be deposited (for example by PECVD, LPCVD, epitaxy and others) or formed inside the substrate (for example by ion exchange, thermal diffusion or ion implantation). It cannot generally be stated which technique is the best. Their selection often depends on whether the device is passive or active and what will be the device application. Based on different considerations, both the materials and an appropriate fabrication technique are chosen according to the desired waveguide characteristics (Nishihara, 1989).

3.1. ION EXCHANGE

Ion exchange is a process where a substrate is immersed in a molten salt or a solution, and the ions present in the liquid phase are exchanged by the ions in the substrate, forming thus a high-refractive-index layer under the surface (Najafi, 1992). For

example, glass waveguides are made by exchanging Na^+ in glass for Ag^+, K^+, Tl^+, and $LiNbO_3$ waveguides are made by exchanging Li^+ for H^+ using benzoic acid. In some cases, an electric field is used for accelerating the ion-exchange process.

In recent years there has been a growing interest in ion exchange technology for the fabrication of passive integrated components. The reason for this is the potential for low-cost, large scale manufacturing together with low losses and compatibility with optical fibers provided by the glass waveguides. In addition, for passive device applications semiconductor detectors have been combined with ion-exchanged waveguides by hybrid integration and by direct deposition of silicon on top of a glass substrate (Tervonen, 1990).

3.1.1. THERMAL ION EXCHANGE

The structure of glass is a network of glass formers, the most common of which are SiO_2 and B_2O_3, modified by other components of the glass composition. The alkali metal oxides present in the glass are in the form of monovalent alkali ions associated with the non-bridging oxygen atoms of the glass structure. These ions have a relatively high mobility at elevated temperatures.

Thermal ion exchange is the simplest method for obtaining low-loss waveguides in glass. A neutral salt containing univalent ions is prepared first. The glass is then immersed in the molten salt for the time needed to exchange Na^+ ions for univalent metal ions near the glass surface. $AgNO_3$ (with a melting point of 208°C), KNO_3 (339°C), and

$TlNO_3$ (230°C) are very often used as the molten salt. The index change Δn near the glass surface is dependent upon the electronic polarizability of the metal ions. Typically, $\Delta n \geq 0.1$ for Tl^+ ions, $\Delta n \approx 2 - 8 \times 10^{-2}$ for Ag^+ ions, and $\Delta n \approx 8 - 20 \times 10^{-3}$ for K^+ ions. The Tl^+ and Ag^+ ion exchanges provide multimode waveguides because the index changes are quite large. On the other hand, the K^+ ion exchange is suitable for fabricating single-mode waveguides.

For Ag^+ and K^+ ion exchange waveguides, $AgNO_3$ or KNO_3 powder is placed in a pyrex crucible and melted in a furnace. A plate of soda-lime glass is then immersed in the molten salt. After the ion exchange, the glass is cooled and the remaining salt adhering to the glass is easily removed with water.

3.1.2. REFRACTIVE INDEX INCREASE FROM ION EXCHANGE

The refractive index profile due to ion exchange (equation 2.16) is a complimentary error function which is the solution of diffusion equation with a constant source (Najafi, 1992).

The effect of the Ag^+-Na^+ -exchange is calculated by replacing a given fraction of Na_2O in the glass by Ag_2O. Ag^+ ions are larger than the Na^+ ions so they can be expected to increase the refractive index of glass because the path length of a photon is larger in the presence of larger ions. This model predicts an approximate empirical relation between the relative Ag^+ concentration, C_{Ag}, and the refractive index increase (Δn_o) (Tervonen, 1990):

$$\Delta n_o = \frac{C_{Ag}}{V_o}\left[\Delta R - \frac{R_o \Delta V}{V_o}\right] \tag{3.1}$$

Here V_o and R_o are, respectively, the volume of glass per gram of oxygen atoms and the refraction per gram of oxygen atoms ($= V_o n_o / C_{Ag}$) in the original composition. ΔV and ΔR are changes of these quantities from the total replacement of Na^+ by Ag^+. For this total replacement the predicted value is $\Delta n_o \approx 0.039$, while the measured maximum index change is about 0.049. The first term in equation 3.1 gives the index change from the increased ionic polarizability. The second term expresses the effect of volume change, in this case the expansion of glass due to a larger radius of Ag^+ ions. The value of these two terms are 0.050 and -0.011, respectively. Since the ion exchange only affects the surface of the glass, the expansion is limited. Glass can only expand in the direction normal to the surface. The swelling of glass at the site of channel waveguides has been observed and investigated (Tervonen, 1990). With a simple assumption of expansion only in one direction, the volume term is one third of that in equation 3.1, and a value $\Delta n \approx 0.047$ is obtained.

An alternative way of looking at the deviation from equation 3.1 caused by compression is the stress-optical effect (Tervonen, 1990). For a planar waveguide, compressive stresses exist in the direction parallel to the surface, while in the direction normal to the surface there is no stress because of the free expansion. This nonisotropic stress causes birefringence, and the index change for the two polarizations are (Tervonen, 1990):

$$\Delta n_{TE} = \Delta n_o + (C_1 + C_2)\, s \tag{3.2}$$

$$\Delta n_{TM} = \Delta n_o + 2\, C_2\, s \tag{3.3}$$

where C_1 and C_2 are the elasto-optic coefficients, and s is the compressive stress in the waveguide. Often only the birefringence factor, the Brewster's constant $B = C_2 - C_1$, is known. Albert and Yip (1987) have shown that for K^+-Na^+ exchange the refractive index increase is mainly due to the induced stress. They also calculated the value for birefringence in potassium-exchanged waveguides, which was close to the measured value. For silver-exchanged waveguides they predicted birefringence factor (B) in the order of 5×10^{-4}.

3.1.3. FABRICATION OF ION-EXCHANGED WAVEGUIDES

There are certain steps that should be respected in the fabrication of ion-exchanged waveguides (Figure 3.1). The glass plates should be plane polished, the surface roughness should be much smaller than the wavelength to be used. The substrate cleaning step must be followed very carefully: the glass substrate is first cleaned by soap and rinsed by water then it is placed for 3 minutes in a warm (40°C) beaker of each of the following liquids: acetone, 1,1,1-trichloroethane, acetone and isopropanol, respectively. Small traces of contamination such as soap from the cleaning step and some metals (for example, silver) can induce undesirable propagation loss or can change Δn from its expected value. The aluminum used for evaporation and the salt for ion exchange must be chosen to be very pure (better than 99.99% by weight purity).

Another important point to consider is to maintain constant temperature during the ion exchange process. The temperature should be chosen such that the ions to be exchanged have their highest mobility (~400°C for potassium ion exchange in BK7 glass). This allows a constant diffusion coefficient during the process. Different diffusion depths can be adjusted by choosing appropriate diffusion time.

The aluminum etcher is a selective etchant that is composed of 80% phosphoric acid, 15% water and 5% nitric acid, and it is used at 25°C. This solution has a very high etch rate for aluminum and a very low etch rate for the photoresist.

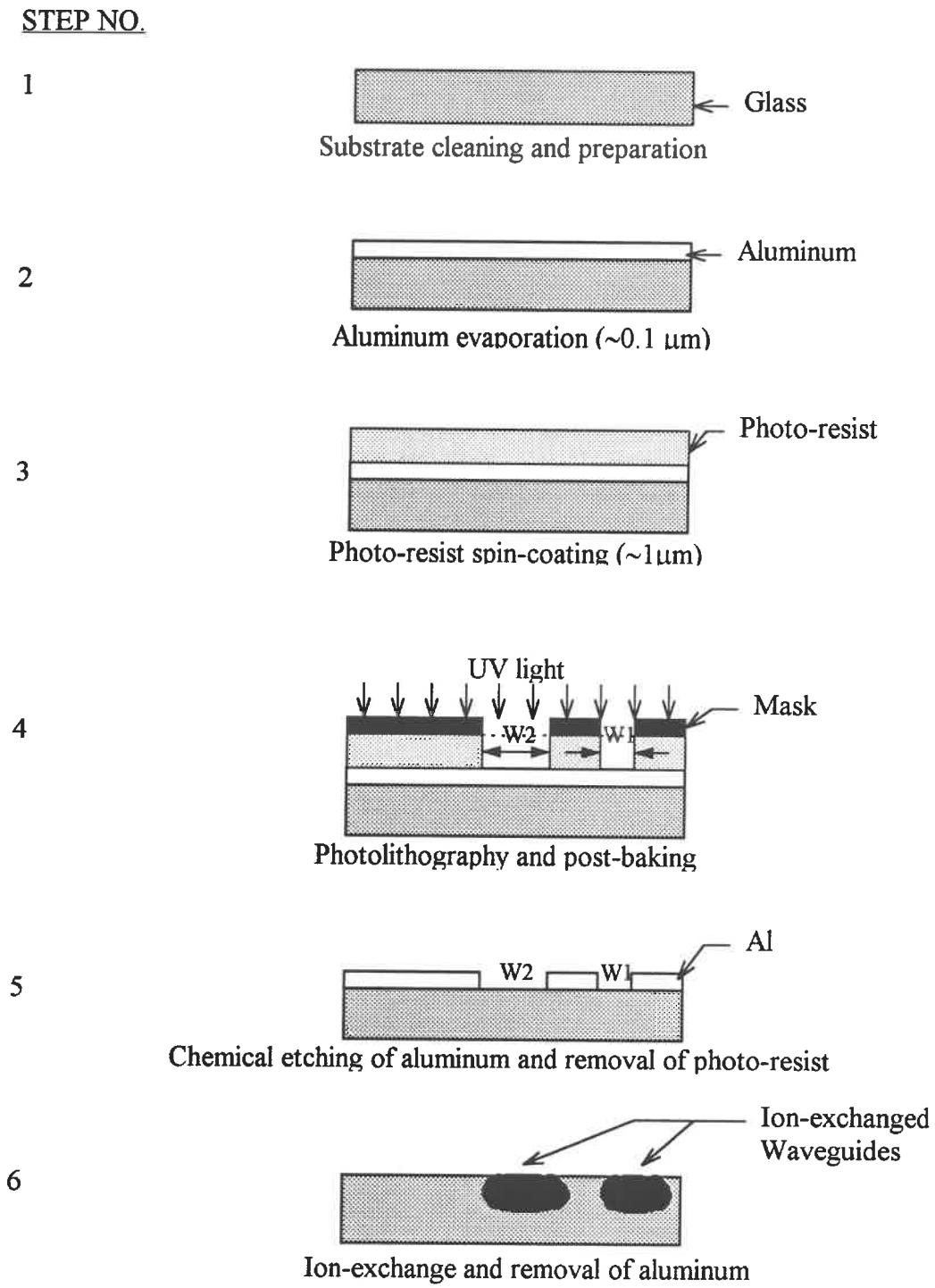

Figure 3.1. Steps in the fabrication of ion-exchanged waveguides.

3.2. PLASMA ENHANCED CHEMICAL VAPOR DEPOSITION

Low pressure plasma processes are very attractive for the fabrication of photonic integrated circuits due to their compatibility with silicon-based microelectronics technology and their suitability for batch- and continuous processing in clean-room facilities. Integration on silicon substrates allows the use of silicon micromachining in fiber pigtailing to photonics devices. Plasma processes can be applied in fabrication of IO devices for the deposition of guiding-, buffer- or cladding layers and for etching. These processes can be performed in the same system and at a relatively low temperature (<300°C) (Martinu, 1996).

3.2.1. PROCESSES IN LOW PRESSURE PLASMA

In the plasma of a low pressure electric discharge, energetic electrons collide with the gas molecules (or atoms) present leading to ionization and to dissociation. Active species (fragments of the dissociated molecules) thus formed diffuse to the substrate surface where they react with each other forming a layer (deposition), or with the substrate forming volatile species (etching).

Hydrogenated amorphous Si-based films such as SiO_2:H, $SiN_{1.3}$:H and SiO_xN_y:H appear to be suitable for the fabrication of optical waveguides. These films are obtained from silane (SiH_4) or from organosilicone compounds (for example hexamethyldisiloxane, $Si_2OC_6H_{18}$) mixed with oxidizing (O_2, N_2O) and/or nitriding (N_2, NH_3) gases. There

exists vast literature on plasma deposition and plasma processing of materials (Mort and Jansen, 1986, Rossnagel et al., 1990).

In general, the physical and chemical reactions in actual plasma are quite complex (Mort et al. , 1990). For example, in a model described by Smith in 1990 the growth of silicon nitride from ammonia and silane mixture takes place by the following steps:

- The ammonia and silane react in the plasma to form a "precursor" molecule, tetra-aminosilane, and hydrogen:

$$SiH_4 + 4NH_3 \rightarrow Si(NH_2)_4 + 4H_2$$

- The precursor molecules deposit on the substrate as $Si(NH_2)_3$ after losing one amino group.
- Neighboring surface molecules condense to form silicon nitride and volatile ammonia.

Silane, SiH_4, is usually used as a silicon source gas, but due to its pyrophoric nature organosilicone compounds such as hexamethyldisiloxane (HMDSO) (Tien et al., 1972) and tetramethylcyclotetrasiloxane (TMCS) (Tabasky et al., 1994) can be considered to replace it. The use of organosilicone monomers usually involves using a carrier gas (e.g. argon) to enhance further dissociation of the monomer and to reduce the residual carbon content.

3.2.2. OPTIMIZATION OF DEPOSITION CONDITIONS

In plasma deposition the film composition is controlled by the feed gas ratios but the film microstructure is a function of surface conditions during film growth, such as

substrate temperature and energy of bombarding ions. The film microstructure (porosity in amorphous films) strongly affects the optical (refractive index) and the mechanical properties (stress, hardness) of the thin film. Higher ion bombardment allows to densify the deposited films without a necessity to substantially increase the substrate temperature. This approach has particularly lead to the development of the dual-mode microwave/radiofrequency (MW/RF) plasma technique (Martinu, 1996).

Figure 3.2 shows the MW/RF plasma system used in this work. RF discharge allows an efficient control of ion bombardment. The plasma bulk potential, V_P, is positive (typically several tens of volts), while a negative d.c. bias voltage, V_B, develops on the RF powered electrode (several hundreds of volts), and V_B is superimposed over the RF signal (Chapman, 1980). This causes ions to be accelerated across the RF-induced plasma sheath to their maximum kinetic energy ($E_i = e|V_P - V_B|$). A dual mode MW/RF plasma combines the advantage of high deposition rate due to the dense MW plasma, while high film density is achieved by applying V_B to the substrate due to the RF signal. In this arrangement a selective control of ion flux, (controlled by the MW power supplied) and of ion energy, E_i, (controlled by V_B) can be achieved (Martinu et al., 1994 and Martinu et al., 1989).

The effect of growth parameters on the evolution of the refractive index of silicon compound films is illustrated in Figure 3.3. For films deposited in MW/RF plasma from $SiH_4/NH_3/N_2O$ mixtures at ambient substrate temperature ($T_s \sim 30°C$) at an ion energy E_i of 160 eV, the refractive index n systematically decreases with increasing N_2O concentration. The resulting n values range from about 1.90 for $SiN_{1.3}$ (using a SiH_4/NH_3

mixture) to 1.46 for SiO_2 (using a SiH_4/N_2O mixture). Deposition at ambient temperature in MW/RF plasma (E_i = 160 eV, T_s ~ 30°C) results in comparable n values as for films obtained in pure microwave plasma (E_i ~ 10 eV, T_s = 280°C) (Blain et al., 1989, see Figure 3.3). Conclusions from Figure 3.3 can be summarized as follows:

(i) The deposition parameters may be chosen so as to obtain the desired n value of the SiO_xN_y films, ranging from that of $SiN_{1.3}$ to that of SiO_2.

(ii) T_s and E_i can be considered interchangeable parameters for density and refractive index of the films.

(iii) The refractive index can be controlled at any given moment of the deposition process, which allows one to deposit multilayer or graded index optical films (Martinu, 1996).

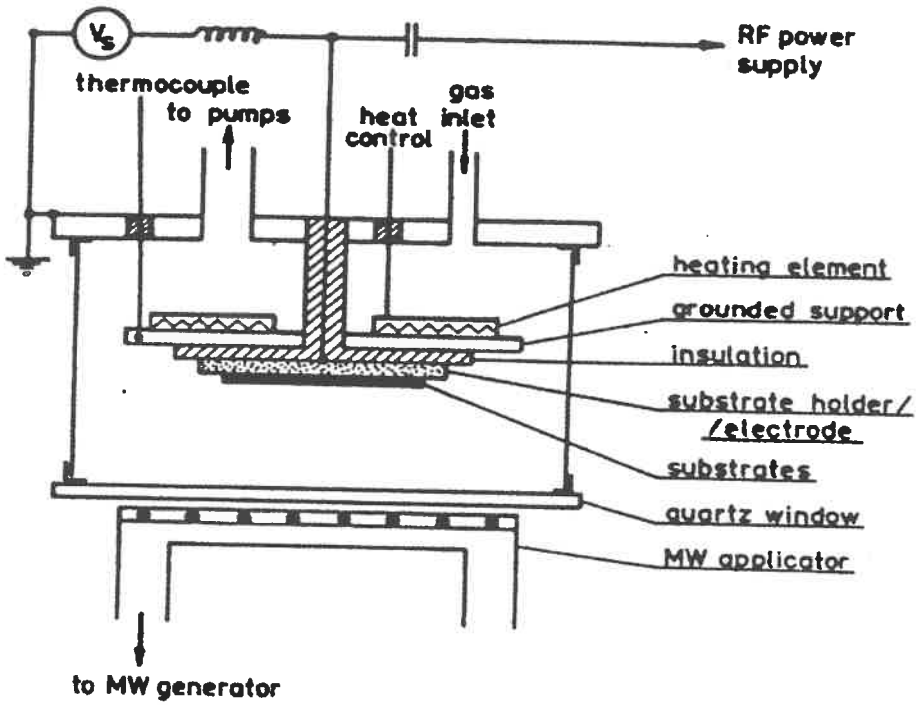

Figure 3.2. Schematic illustration of a dual-mode microwave/radiofrequency (MW/RF) plasma reactor (Martinu, 1996).

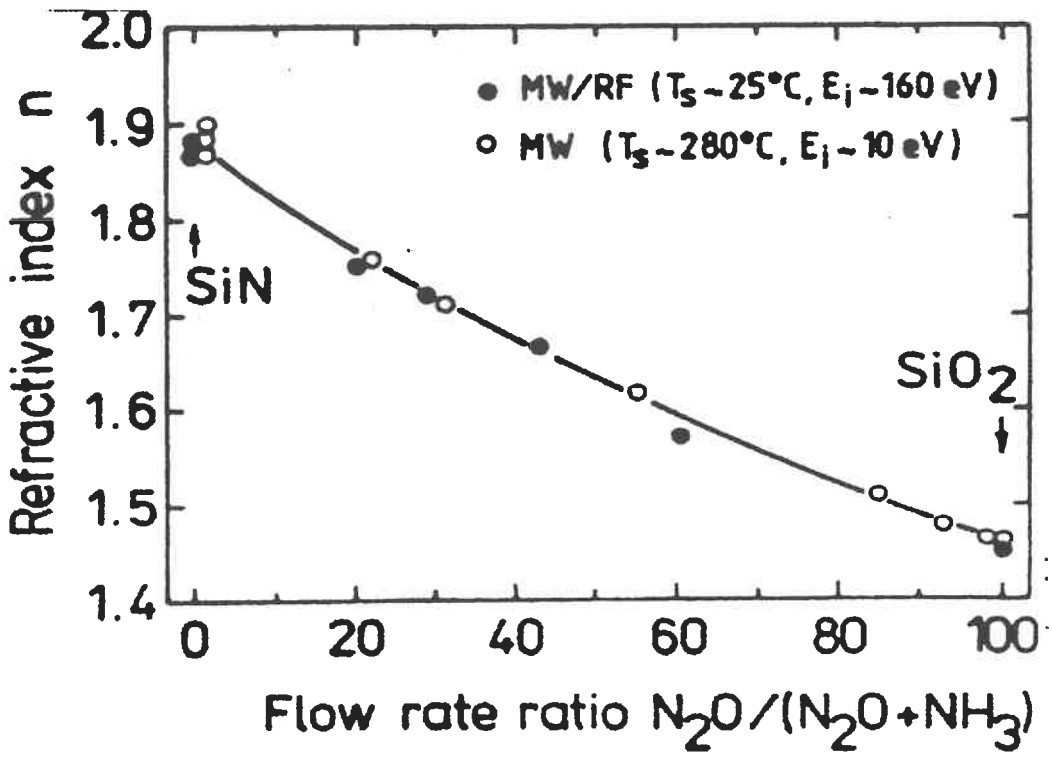

Figure 3.3. Refractive index (at λ~600 nm) of SiO_xN_y films deposited in a MW/RF plasma as a function of N_2O /(N_2O + NH_3) gas flow ratio (•) (after Poitras et al.). For comparison, the results from a pure MW discharge using T_s=280°C (o) are shown (after Blain et al., 1989).

3.2.3. RIDGE WAVEGUIDE FABRICATION USING PECVD

One can fabricate ridge waveguides using PECVD of silicon oxynitride films, the material of choice in this work (Figure 3.4). Ridge waveguides are surrounded from three sides by the upper cladding and therefore they provide a higher sensitivity of IO sensors as we will see in the next chapter. Ridge waveguides are fabricated by a lithography process using reactive ion etching (RIE) as illustrated in Figure 3.4.

3.3. WAVEGUIDE CHARACTERIZATION

Waveguide characterization involves the determination of waveguide dimensions, and their refractive index and propagation loss. This information is required when designing any waveguide device.

For the ridge waveguides the dimensions can be measured directly using profilometry or scanning electron microscopy. In the case of ion-exchanged waveguides the picture is more complex because the refractive index increases gradually; therefore, waveguide depth (d) is the distance at which the refractive index attains 1/e of its value at the waveguide surface, and this information can be found by prism coupling and by the WKB method.

STEP NO.

1

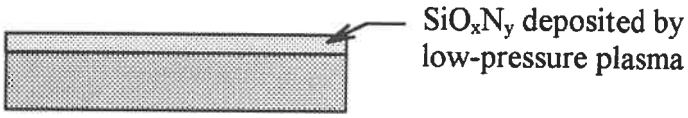

Deposition of a thin film by PECVD

2

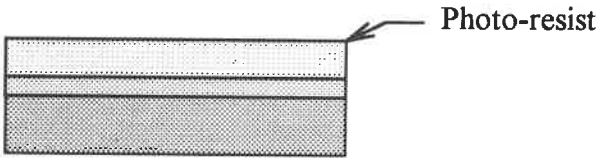

Spin-coating the photo-resist

3

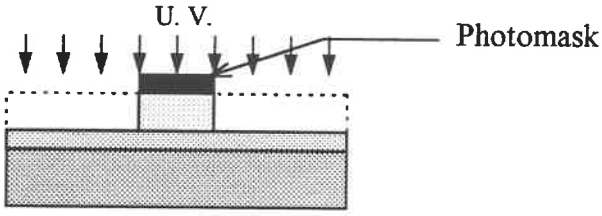

Photolithography and post-baking

4

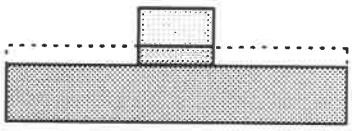

Reactive ion etching (RIE)

5

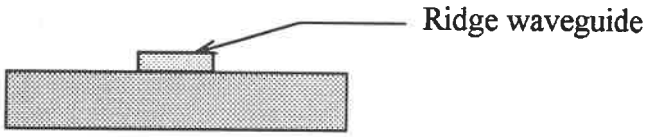

Removal of photoresist

Figure 3.4. Fabrication steps of ridge waveguide prepared by PECVD.

3.3.1. PRISM COUPLING METHOD

This is a simple and unique method for finding the effective refractive indices of slab or buried channel waveguides. It cannot be used for ridge waveguides because they could be damaged.

In this method a prism with a refractive index slightly higher than the guiding layer of the waveguide is placed in optical contact with the waveguide (Figure 3.5). Then a polarized light beam is directed to the large face of the prism since the effective index for the TE-polarized light is different from the effective index for the TM-polarized light. The angle θ between the normal to the prism and the incident light beam is changed gradually until a mode in the waveguide is excited and the mode's M-line is observed on a screen or by a photodetector. At this moment, the phase matching between the incident wave and the guided mode occurs. Using the following formula, one can calculate the effective index corresponding to the mth mode (Najafi, 1992):

$$N_m = n_p \sin\left(\arcsin\left(\frac{\sin(\theta_m)}{n_p}\right) + \alpha\right) \tag{3.4}$$

where θ_m is the angle of incidence, n_p is the refractive index of the prism and α is the "Toe" angle of the prism. This is a nondestructive method for buried waveguides. This method has a very high precision (± 0.0001) for the measured effective indices.

3.3.2. GRATING METHOD

The grating method (Figure 3.6) is suitable for finding effective indices of a ridge waveguide. It is a destructive method. The grating with a period Λ at the surface of the waveguide generates a small perturbation to a mode (guided or radiation mode) of the waveguide. This causes coupling of the light from one mode to another mode determined by the phase matching condition. When phase matching has taken place between a guided mode and a radiation mode, an efficient transfer of power between these two modes occurs. The phase matching condition in this case can be written as (Najafi, 1992):

$$\beta_m = \beta_r + \frac{2j\pi}{\Lambda} \qquad j = 0, \pm 1, \pm 2, \ldots \tag{3.5}$$

where $\beta_m=(2\ \pi\ /\ \lambda)N_m$ and $\beta_r=(2\ \pi\ /\ \lambda)\ \sin(\theta_m)$ are the propagation constants of the guided mode and of the radiation mode. In this case the effective refractive index N_m can be expressed as:

$$N_m = \sin(\theta_m) + \frac{\lambda}{\Lambda} \tag{3.6}$$

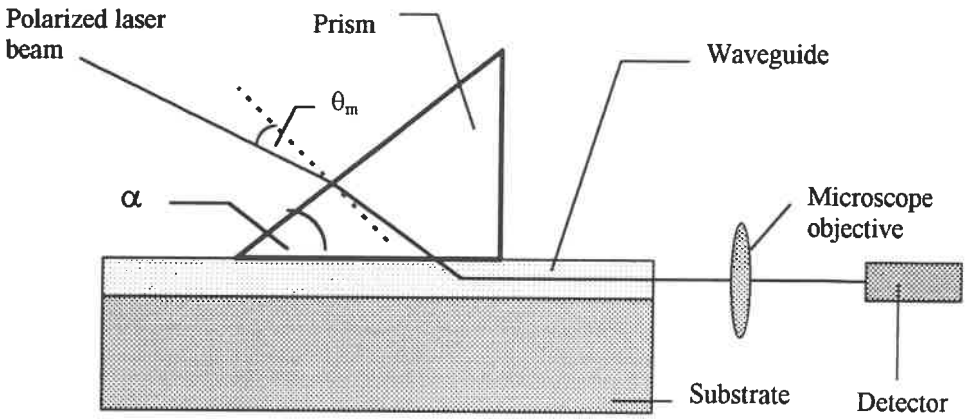

Figure 3.5. Prism coupling for measuring effective indices of modes.

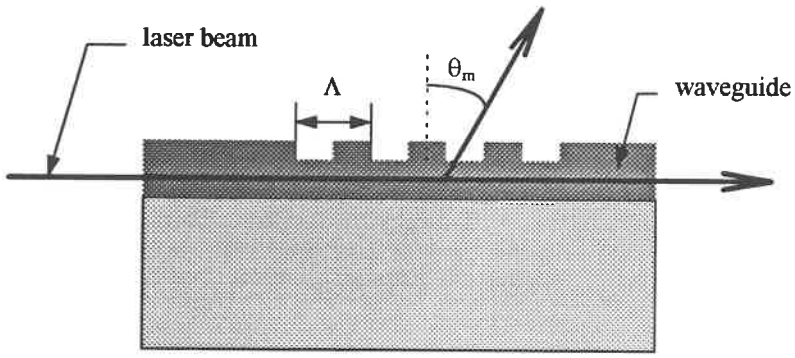

Figure 3.6. Grating method for measuring effective indices of modes.

3.3.3. TRANSMISSION AND REFLECTION METHOD

Transmission and reflection of a thin film (slab waveguide) is a function of film thickness and refractive index. One can simulate transmission and reflection given an initial trial of thickness and refractive index for a given substrate refractive index, wavelength and angle of incidence (Eckertova, 1986). On the other hand, the experimental transmission and reflection can be measured using a spectrophotometer. The thickness and refractive index should be iteratively changed to find a minimum merit function (difference between simulated and measured transmission and reflection).

There is an important limitation to this method. The merit function can have more than one minimum, and we should be looking for a global minimum. To achieve this we should either have initial values very close to the actual values or we should utilize a global optimization technique.

This method can be expanded to find the refractive index over a broad range of wavelengths using different dispersion curves describing the continuity of the optical constants over a certain wavelength range. For example, Sellmeier formula (Tatian, 1984):

$$n(\lambda)^2 = 1 + \sum_{j=1}^{k} \frac{A_j \lambda^2}{\lambda^2 - B_j^2} \tag{3.7}$$

where $n(\lambda)$ is the refractive index at wavelength λ, A_j, and B_j are the constants to be determined by the fitting process.

Figure 3.7 shows the refractive index of thin films of $SiN_{1.3}$, SiO_xN_y and SiO_2 deposited by low pressure plasma. The program used for these optimizations is the Filmstar software package[1].

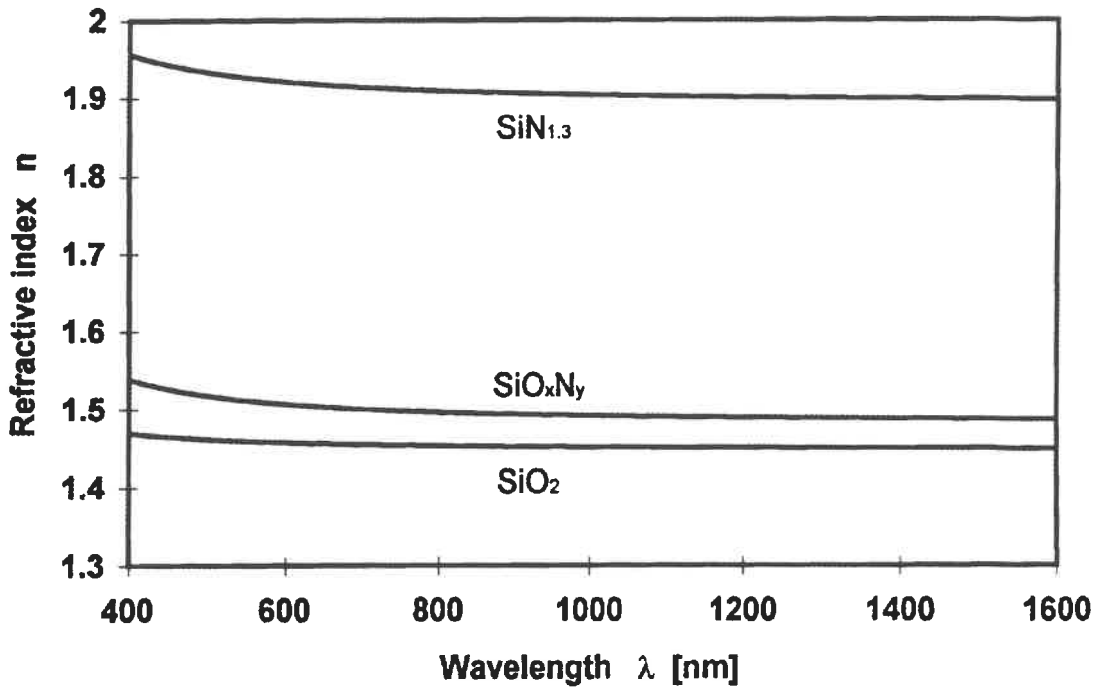

Figure 3.7. Typical refractive index dispersion curves SiO_2, SiO_xN_y and $SiN_{1.3}$ films deposited in MW/RF plasma.

[1] Thin film design and optimization software, FTG Software Associates, Princeton, NJ, USA

3.3.4. LOSS MEASUREMENT

Optical loss is an important parameter in the operation of integrated optical devices, since it characterizes the amount of energy lost in the devices by absorption, scattering, radiation and coupling. The unit of propagation loss is dB/cm, and it can be found using the following formula:

$$\text{Loss} = \frac{10\log(P_0/P_1)}{z_1 - z_0}\,(\text{dB/cm}) \tag{3.8}$$

where P_o and P_1 are the optical power at the positions z_o and z_1 of a waveguide (see Figures 3.8 and 3.9).

3.3.4.1. END-COUPLING METHOD

The end-coupling method is a simple and accurate method for measuring the propagation and coupling loss separately. The measurement setup is shown in Figure 3.8. The power P_o from the input fiber is sent through a microscope objective M and is measured by a detector. Then the same power P_o is coupled into the waveguide whose loss characteristics are to be measured. The output of the waveguide is coupled into a monomode fiber, the same type as the input fiber, and the output P_2 is measured through the objective M. Finally, the output P_3 of the waveguide is sent through the objective M and measured. These measurements give us two equations for two unknowns (Wang et al., 1993):

$$P_2 = P_0(1-\alpha_c)^2(1-\alpha_p) \tag{3.9}$$

$$P_3 = P_o(1-\alpha_c)(1-\alpha_p)T_f \tag{3.10}$$

where α_p and α_c are the propagation and coupling losses, and T_f is the transmission of the fiber that can be easily measured.

3.3.4.2. SCATTERED LIGHT MEASUREMENT METHOD

In a waveguide, a guided mode continuously loses a small part of its power by Rayleigh scattering. This scattered power is proportional to the total guided power. Thus the decrease in the scattered light shows the propagation losses of the guided mode.

The measurement setup is shown in Figure 3.9 (Najafi, 1992). The scanning fiber should be multimode to collect the light from a relatively wide angle (~70°). The steps for reading the scattered power should be quite small (~0.1 mm) to provide data with a good resolution. At each step, the lateral position of the scanning fiber should be fine-tuned to have a maximum scattered light reading. The distance between the scanning fiber and the waveguide should be kept constant; this is accomplished by adjusting the sample holder parallel to the micropositioner.

The scattered light decreases exponentially along the waveguide. By fitting the measured scattered power to a decreasing exponential function, the attenuation coefficient is obtained. The accuracy (close to ±0.1 dB/cm) depends on the sensitivity of the detection system. The power coupled to the waveguide should be kept constant during the loss measurement. To do this the output of the waveguide can be monitored. The non-uniformities in the scattered radiation can be due to a change in the coupling of

light into the waveguide or a change in the distance of the scanning fiber and waveguide during measurement.

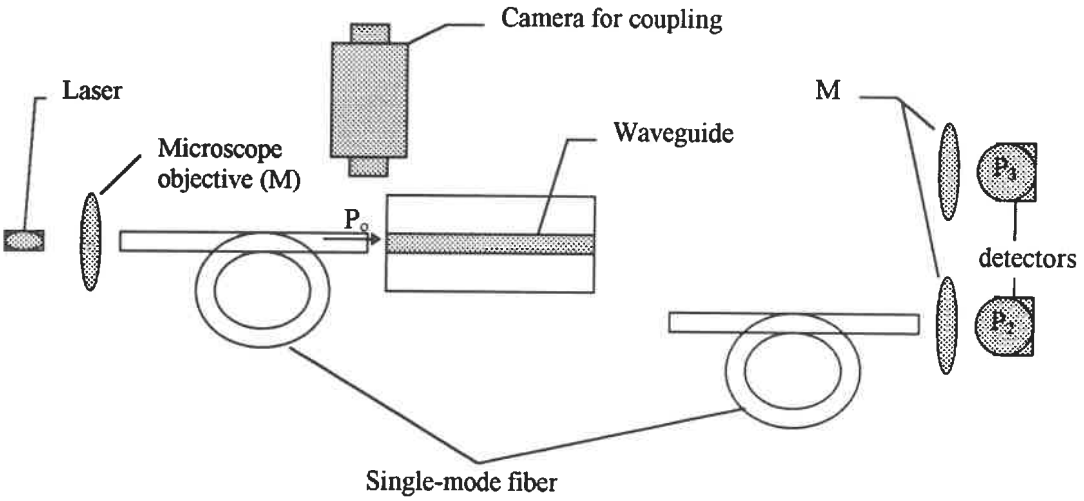

Figure 3.8. Loss measurement using fiber end-coupling.

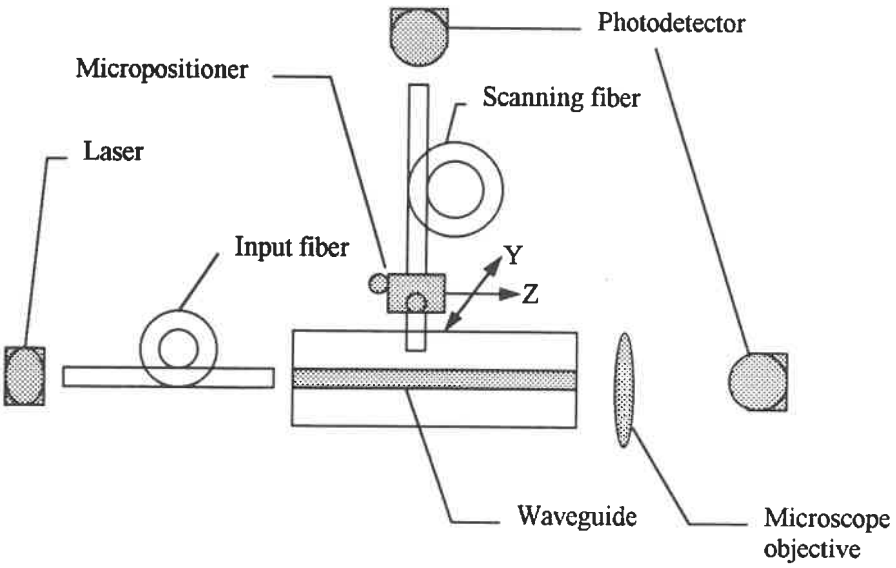

Figure 3.9. Loss measurement by scattered light.

CHAPTER 4

WAVEGUIDE FABRICATION AND CHARACTERIZATION: RESULTS

This chapter summarizes the results from fabrication and characterization of the studied waveguides. These results are discussed in terms of their relevance to the design and function of the sensor. The waveguides were fabricated using K^+-exchange and PECVD.

4.1. K^+-EXCHANGE WAVEGUIDES

The potassium ion-exchange technique described in Chapter 3 is now applied for the fabrication of low-loss waveguides in BK7 glass.

Firstly, BK7 substrates were cleaned as described in section 3.1.3. A thin film of pure (99.9999%) aluminum (~0.1 μm) was evaporated onto the substrates. Substrates were then coated by photoresist, and the photolithography process with a straight-waveguide mask was performed. The samples were placed in an aluminum etcher (80% phosphoric acid, 5% nitric acid, 15% water) for 3 minutes. The aluminum etcher does not etch the photoresist. Photoresist was afterwards removed using acetone, and the samples were closely observed under the microscope to make sure that aluminum covers everywhere except the waveguide openings. Then the samples were placed in pure KNO_3 which was already melted in a furnace. Some BK7 glasses without Al-mask were also

placed in the furnace to fabricate slab waveguides at the same time. The temperature during ion-exchange was kept at 400°C and the process was continued for 25 hours. The samples were taken out of the oven and aluminum was removed. The two side edges of the samples were polished to facilitate coupling of light into the waveguides.

Prism coupling was used as a method to measure effective refractive indices in the samples with channel waveguides (Tables 4.1 through 4.4) and slab waveguides (Table 4.5).

For slab waveguides, the WKB method was exploited to obtain the maximum index change (Δn) and the refractive index profile depth (d). Δn and d were found to be 0.0081±0.0001 and 16.55±0.01 μm for TE-polarization, and 0.0110±0.0001 and 15.14 ±0.01 μm for the TM-polarization, respectively.

For the channel waveguides, the effective index method was used to simulate the effective indices of the ion-exchanged waveguides at the wavelengths of the HeNe and Nd:YAG lasers ($\lambda_1 = 0.6328$ μm, $\lambda_2 = 1.0639$ μm). The calculated effective indices were compared with the experimental effective indices. The parameters Δn and d were changed and effective indices were calculated again. This process of optimization was repeated until the best match between theory and experiment was found. Δn for the channel waveguides was found to be the same as Δn for the slab waveguides, but d and the diffusion coefficient D were found to decrease with decreasing the mask width (Table 4.6). This dependence of d and D on the aluminum mask width can be explained in terms

of electrostratic interaction between the charges on the aluminum mask and the exchanged ions. Therefore, we refer to D as apparent diffusion coefficient.

In designing the sensor, Δn and d play a very important role: d is related to the potassium apparent diffusion coefficient D and diffusion time t by a simple relation: $d = \sqrt{Dt}$. For a mask with waveguide openings of different widths, the diffusion coefficients were calculated (Table 4.6). Knowing the diffusion coefficient, we can choose the diffusion time in such a way to obtain single-mode waveguide and to have a considerable amount of the propagated power in the cladding for enhancement of the sensor's sensitivity.

Table 4.1. Prism coupling results (effective index, N_m) for K^+-exchanged channel waveguides (t = 25 hours) with different mask openings (W) and for different modes of propagation (m) at the HeNe laser (λ=0.6328 μm) wavelength (TE-polarization) and n_s (λ = 0.6328 μm) = 1.5151.

TE-Polarization	m=0	m=1	m=2	m=3
W=8 μm	1.5207	1.5201	1.5184	1.5170
W=7 μm	1.5203	1.5196	1.5181	1.5167
W=6 μm	1.5200	1.5181	1.5170	1.5167
W=5 μm	1.5195	1.5185	1.5178	1.5172
W=4 μm	1.5192	1.5181	1.5175	1.5167
W=3 μm	1.5190	1.5180	1.5173	1.5165

Table 4.2. Prism coupling results (effective index, N_m) for K^+-exchanged channel waveguides (t = 25 hours) with different mask openings (W) and for different modes of propagation (m) at the HeNe laser (λ=0.6328 μm) wavelength. (TM-polarization) and n_s (λ=0.6328 μm) = 1.5151.

TM-Polarization	m=0	m=1	m=2	m=3
W=8 μm	1.5199	1.5188	1.5180	1.5173
W=7 μm	1.5195	1.5190	1.5175	1.5169
W=6 μm	1.5194	1.5185	1.5174	1.5168
W=5 μm	1.5190	1.5183	1.5174	1.5168
W=4 μm	1.5189	1.5179	1.5174	1.5165
W=3 μm	1.5186	1.5180	1.5173	1.5165

Table 4.3. Prism coupling results (effective index, N_m) for K^+-exchanged channel waveguides (t = 25 hours) with different mask openings (W) and for fundamental mode (m_o) at the Nd:YAG laser (λ = 1.0639 μm) wavelength (TE-polarization) and n_s (λ = 1.0639 μm) = 1.5065.

TE-Polarization	m=0
W=8 μm	1.5086
W=7 μm	1.5084
W=6 μm	1.5082
W=5 μm	1.5080
W=4 μm	1.5078
W= 3 μm	1.5074

Table 4.4. Prism coupling results (effective index, N_m) for K^+-exchanged channel waveguides (t = 25 hours) with different mask openings (W) and for fundamental mode (m_o) at the Nd:YAG laser (λ = 1.0639 μm) wavelength (TM-polarization) and n_s (λ =1.0639 μm) = 1.5065.

TM-Polarization	m=0
W=8 μm	1.5088
W=7 μm	1.5086
W=6 μm	1.5086
W=5 μm	1.5085
W=4 μm	1.5083
W=3 μm	1.5080

Table 4.5. Prism coupling results (effective index, N_m) for K^+-exchanged slab waveguides (t = 25 hours) for different modes of propagation (m) at the HeNe laser (λ = 0.6328 μm) wavelength and n_s (λ = 0.6328 μm) = 1.5151.

	TE-Polarization	TM-Polarization
m=0	1.5209	1.5227
m=1	1.5190	1.5207
m=2	1.5180	1.5191
m=3	1.5170	1.5178

Table 4.6. d, Δn and the apparent diffusion coefficient (D) values obtained for the K^+-exchanged channel waveguides (t = 25 hours, TM-polarization).

TM	W = 8 μm	W = 7 μm	W = 6 μm	W = 5 μm	W = 4 μm
d (μm)	12	11	10	9	8
Δn	0.0110	0.0110	0.0110	0.0110	0.0110
D(μm^2/h)	5.76	4.84	4.00	3.24	2.56

4.2. PECVD SiO_xN_y WAVEGUIDES

Fabrication of PECVD waveguides on silicon allows to eliminate the polishing step which is the most costly one in the fabrication of optical integrated circuits. The devices fabricated by this method can operate at high temperature (up to ~1000°C) while this is impossible for ion-exchanged devices.

Silicon wafers with a 2.0 μm thermally grown oxide were used as substrates, and SiO_xN_y thin films were deposited at T_s = 30°C. The flow rates for SiH_4, N_2O and NH_3 were 6, 12 and 4 standard cubic centimeters per minute (sccm), respectively, with the aim to obtain Δn of about 0.08. The power was 30 Watts, the bias voltage was 160 Volts and the deposition rate was about 1 μm/h. The refractive index dispersion for the films and for the thermal oxide was measured using the method discussed in section 3.3.3 (Figures 4.1 and 4.2).

The samples were cleaned, OCG® photoresist was spin coated, and photolithography was performed. The exposure time to UV was 30 seconds and the softbake and the hardbake were 30 minutes each at temperatures of 90°C and of 110°C, respectively. Afterwards, the samples were etched using reactive ion etching (RIE) in the same system as illustrated in Figure 3.2, using only an RF discharge. The gas used for etching was CF_4, the etching rate was 0.1 μm/min and the supplied power was 60 Watts. The propagation loss was measured using the scattered light method for waveguides fabricated at the same conditions (see section 4.2) but with different mask openings W (see Figures 4.4 and 4.5). The propagation loss was found between 5.0 to 7.6 dB/cm for the SiO_xN_y waveguides fabricated at the ambient substrate temperature with high ion bombardment. These loss values are relatively high for making devices longer than one cm, and they are mainly caused by internal inhomogeneity (columnar structure, voids). Therefore, the substrate temperature should be increased for further densification. In fact, plasma-deposited waveguides at high substrate temperature (T_s = 200-300°C) were reported having propagation loss equal to 1.14 dB/cm (Sriram et al., 1983). Loss of 1.5 dB/cm and 0.6 dB/cm were reported for silicon oxynitride waveguides fabricated at T_s= 200°C and T_s=300°C, respectively (Lam, 1984, Kapser et al., 1991). Figure 4.3 shows the samples after etching. One can easily observe that the surface roughness in these waveguides is smaller than a fraction of a micron; it is therefore surmised that surface scattering cannot be the main source of the high propagation loss.

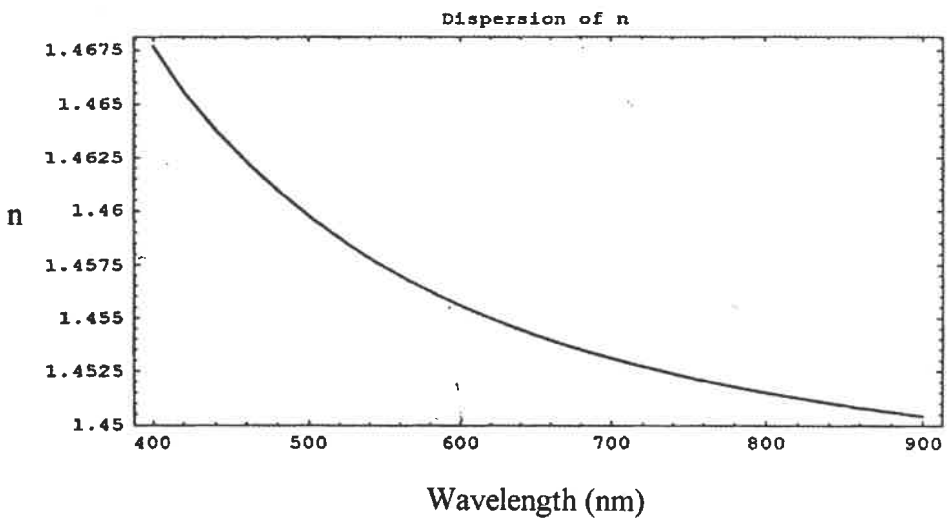

Figure 4.1. Refractive index dispersion found for thermally grown SiO_2.

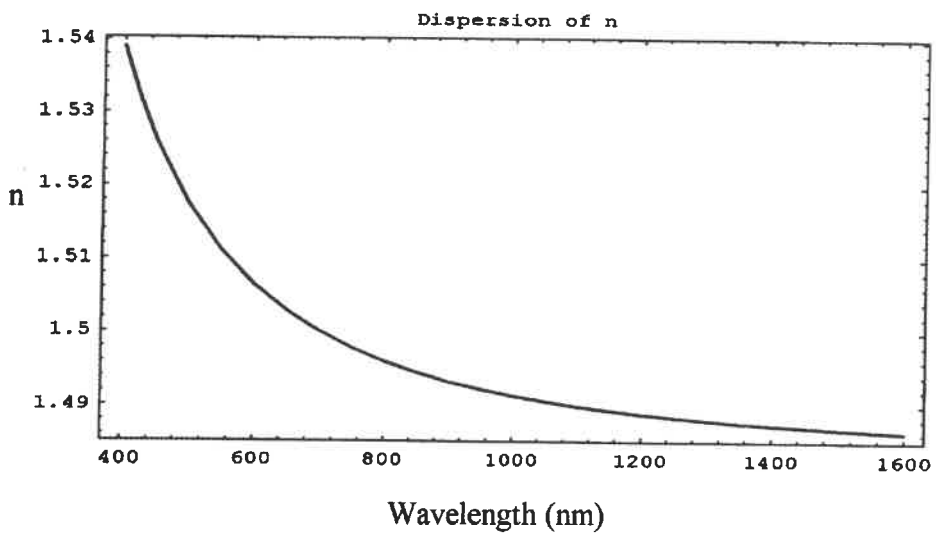

Figure 4.2. Refractive index dispersion found for SiO_xN_y deposited by PECVD.

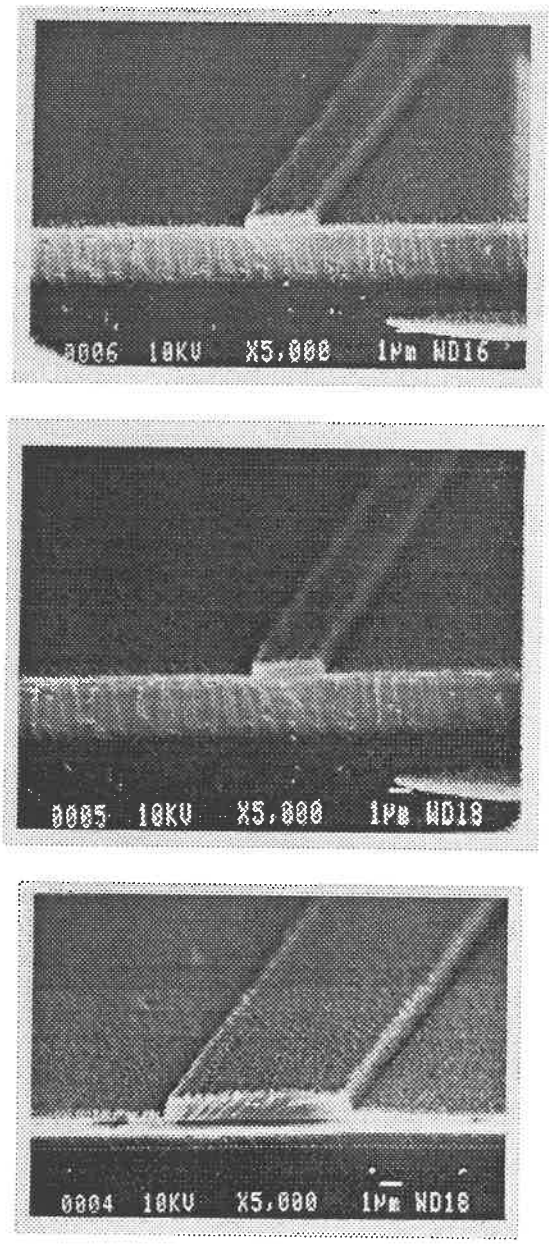

Figure 4.3. SEM micrographs of ridge waveguides fabricated from the same PECVD SiO_xN_y film using masks with different openings: W = 2 μm (the first two), and W = 6 μm (the last).

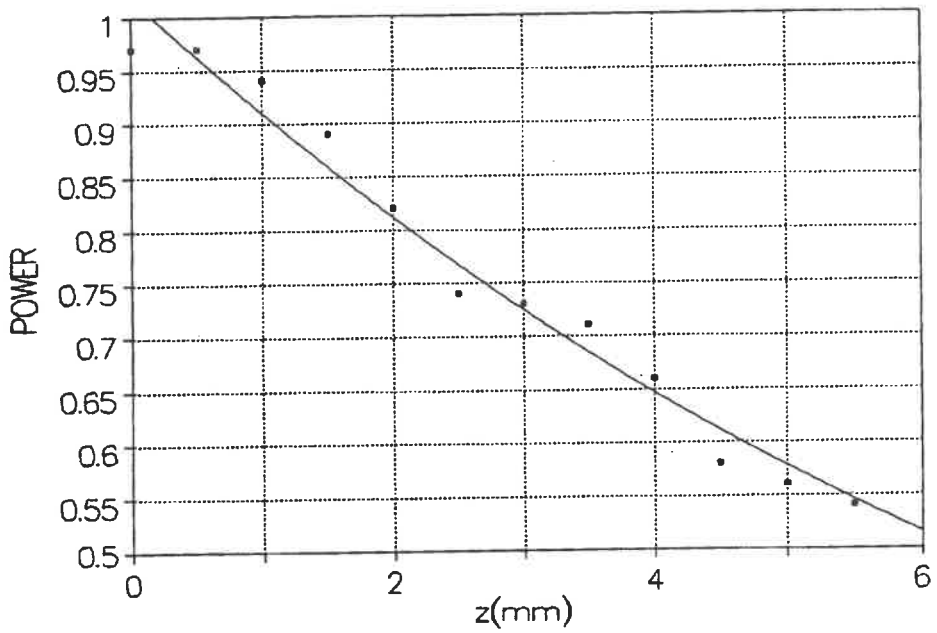

Figure 4.4. Scattered light measurement result in μW for PECVD SiO_xN_y ridge waveguide deposited at ambient substrate temperature and using W = 6 μm as in Figure 4.3. The solid curve is an exponential fit of the experimental points. Propagation loss ≅ 5.0±0.1 dB/cm.

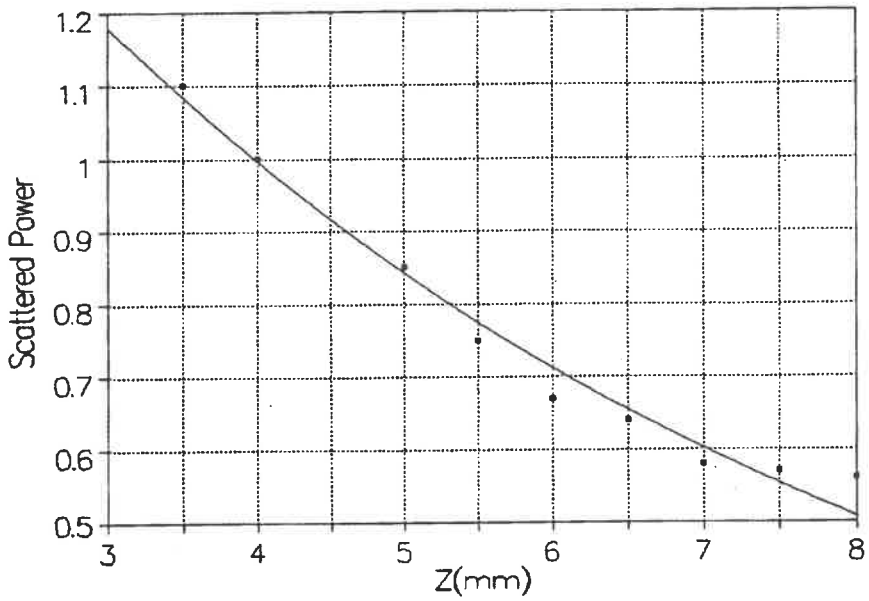

Figure 4.5. Scattered light measurement result in μW for PECVD SiO_xN_y ridge waveguide deposited at ambient substrate temperature and using W = 2 μm as in Figure 4.3. The solid curve is an exponential fit of the experimental points. Propagation loss ≅ 7.6±0.1 dB/cm.

CHAPTER 5

COMPARISON OF DIFFERENT MACH-ZEHNDER INTERFEROMETER SENSORS

MZI is a device for measuring the phase of the propagated mode in a waveguide. This is achieved by superposing the mode with the mode in a reference arm. The level of power in the output is related to the phase difference.

This chapter covers all aspects regarding design and simulation of the sensor and a comparison between different types of this sensor. We have studied theoretically the performance of symmetric and nonsymmetric MZI sensors with ridge and buried index profiles. The effect of device parameters (in particular window opening in symmetric and path length difference in nonsymmetric interferometers) on sensor performance is investigated. Sensors with low losses are designed based on the previously measured materials characteristics.

5.1. TWO-BEAM INTERFEROMETRY

Two-beam interferometry allows the measurement of an extremely small differential phase shift in the optical waveguide generated by the measured medium. The optical phase delay (in radian) of light passing through a waveguide is given by:

$$\phi = NkL \tag{5.1}$$

where N is the effective refractive index of the mode in the waveguide, k is the optical wave-number in vacuum ($2\pi/\lambda$, λ being the wavelength), and L is the physical length of the waveguide. It can be seen that the value of ϕ may depend on the polarization of the output light selected (as although $L_1 = L_2 = L$, for different polarization modes, effective indices in the two branches are different, due to the waveguide birefringence) (Snyder et al., 1983).

Small variations in the phase delay are found by differentiation of equation 5.1.

$$\frac{d\phi}{\phi} = \frac{dL}{L} + \frac{dN}{N} + \frac{dk}{k} \tag{5.2}$$

The first two terms are related to the physical changes in the waveguide caused by the perturbation to be measured (Udd, 1991).

5.2. DEVICE STRUCTURE

Figure 5.1 shows the four different MZI layouts and their corresponding active region refractive index profile studied in this work and their corresponding active region index profiles. The present design of interferometers considers refractive indices of films fabricated by PECVD, using SiO_2 and silicon oxynitrides deposited onto a silicon substrate.

MZ1 , MZ3, and MZ4 are symmetric interferometers with a window of length l. Cladding with a refractive index of 1.4931 (corresponding to liquids such as Toluene or Benzene) covers the surface of the interferometers, except for the window regions which

are exposed to an analyte. MZ2 is nonsymmetric with a path-length difference Δl between the two arms. MZ2 is completely exposed to the analyte.

The radius of curvature ($R_c = 4$ cm) in the interferometers is kept constant in all of the devices; the devices may have slightly different length (L). R_c is optimized to have small bending losses (~0.2 dB/cm).

In MZ4, the coupling length (L_c) is the minimum length for which total coupling occurs (Malek-Tabrizi et al., 1996):

$$L_c = \frac{\lambda}{\beta_{even} - \beta_{odd}} \tag{5.3}$$

β_{even} and β_{odd} are the propagation constants for even and odd modes in the coupling region. L_c is found to be ~1600 μm in our device. An even mode is the one whose electric field is symmetric with respect to the xz or yz planes in a waveguide, an odd mode is the one whose electric field is a negative value of its mirror image in the xz or yz planes (see Figure 2.1).

The guiding layer is separated from the silicon substrate by a 2 μm thick buffer layer (see figure 5.1). This thickness provides sufficient distance for the evanescent field of the guided mode to vanish before encountering silicon. Otherwise, the high refractive index and absorption coefficient of silicon could lead to a considerable loss.

All of the index profiles are designed to provide single-mode propagation except for the Y-junctions. In the active region of the device and the refractive index of the analyte (n_{sup}) should not shift the device out of single-mode regime, i.e., the following condition should apply (Nishihara et al., 1989):

$$\text{(Multimode regime)} \quad 1.491 < n_{sup} < 1.498 \quad \text{(Cut-off)}. \tag{5.4}$$

The two limiting values for multimode and cut-off regimes are estimated using EIM (see section 2.6).

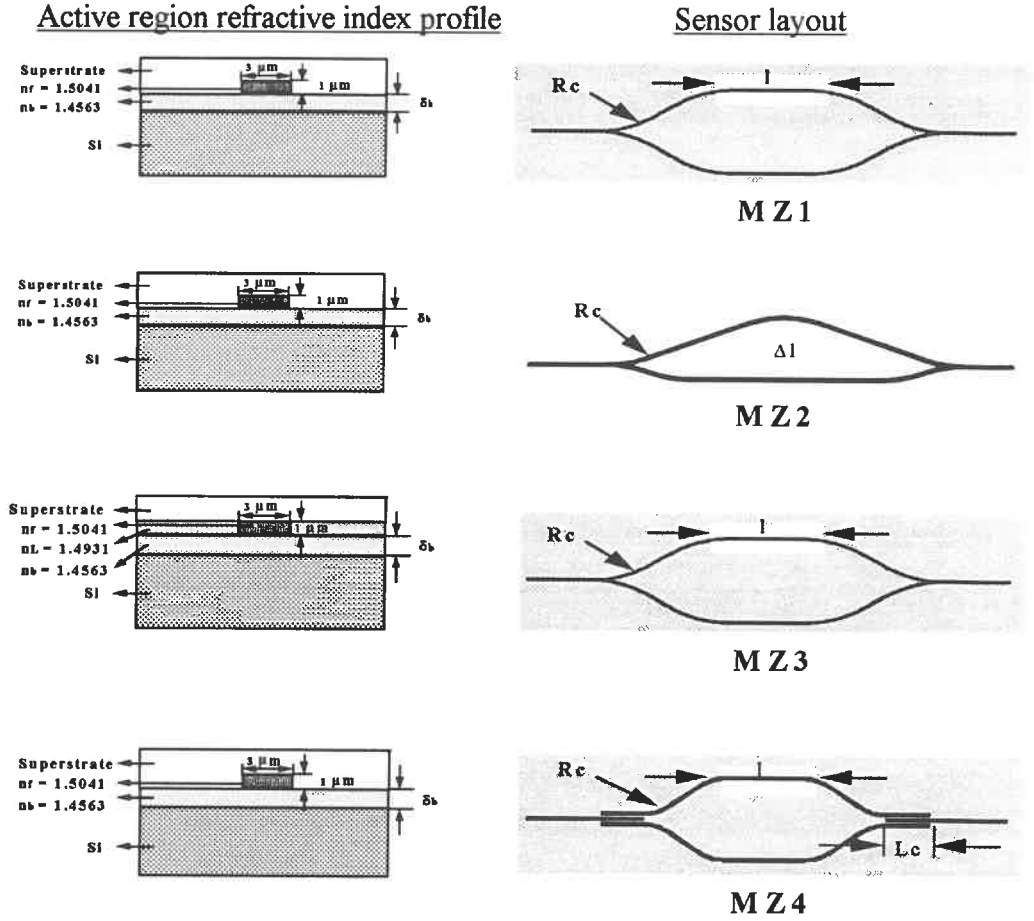

Figure 5.1. Schematic illustration of different Mach-Zehnder interferometers and their active region refractive index profile (Malek-Tabrizi et al., 1996).

This range can be shifted according to the refractive index profile and waveguide dimensions chosen (see Chapter 2). One could obtain a wider dynamic range if the chosen refractive index assures the existance of a weakly-guided mode, but this would decrease the sensitivity of the sensor (Malek-Tabrizi et al., 1996).

5.3. DEVICE OPERATION

In MZI, the fundamental mode from the single-mode input waveguide equally excites the fundamental modes in the two single-mode branches. In symmetric MZIs, there is no path length difference (Δl) between the two branches. The phase difference, $\Delta\Phi$, between the two branches is caused by a difference in the effective refractive indices,

$$\Delta\phi(\text{symmetric}) = \frac{2\pi}{\lambda} l \left| N_{eff}(\text{reference}) - N_{eff}(\text{active region}) \right| \tag{5.5}$$

In our calculations the wavelength, λ, is selected to be 0.633 μm.

In a nonsymmetric MZI, an intrinsic path length difference between the two branches is deliberately created. The phase difference between the two branches is further affected by the refractive index of the surrounding medium, thus modifying the effective refractive index of the whole device:

$$\Delta\phi(\text{nonsymmetric}) = \frac{2\pi}{\lambda} \Delta l \left| N^{i}_{eff} - N^{f}_{eff} \right| \tag{5.6}$$

where N^{i}_{eff} is the initial effective refractive index, and N^{f}_{eff} is the effective refractive index after exposing the device to the analyte.

The effective refractive index of a waveguide is a function of the refractive index of the superstrate (Helmers et al., 1996). This dependence is stronger for a weakly guided design (near cut-off) because the evanescent tail of a weakly guided mode is longer (Helmers et al., 1996). Figures 5.2a to 5.2d represent FD-BPM simulation of MZ1 and MZ4 in two extreme cases of constructive and destructive interference. The two modes in the two branches equally excite odd and even modes when they reach the output Y-branch or the coupler. Even modes of the Y-branch or the coupler region have phases equal to that of their incoming modes, and the odd modes' phase difference is shifted by 180° compared to the phase difference of the incoming modes. Therefore, if there are two incoming modes with a phase difference of 0°, they excite even modes that interfere constructively, and odd modes that interfere destructively (see Figures 5.2b and 5.2d). The even mode of the Y-branch or the coupler region excites the output waveguide, and a maximum output power is measured. On the contrary, if there is a 180° phase difference between the incoming modes in the Y-branch or the coupler, the even modes will interfere destructively and the odd modes interfere constructively (Figures 5.2a and 5.2c). The odd mode is absorbed by the substrate or it is radiated away, and consequently a minimum output power is detected.

In a MZI, the output and input powers are related as (Udd, 1991):

$$\frac{P_{out}}{P_{in}} = \frac{\gamma}{2}\left[1 + m\mathrm{Cos}(\Delta\Phi)\right] \tag{5.7}$$

The quantities γ and m are related to the insertion loss and the propagation loss of the interferometer, respectively. P_{out} and P_{in} are output and input powers, respectively (Malek-Tabrizi et al, 1996).

Sensitivity of the sensor can be defined as the degree of the dependence of the output on the refractive index of the superstrate i.e. the slope of the output curve. We can see that sensitivity has its maximum far from the constructive or destructive interference points (Figures 5.3, 5.4, 5.5, 5.6).

5.4. DISCUSSION

Figures 5.3, 5.4, 5.5 and 5.6 are the results of the FD-BPM simulations of the devices from Figure 5.1. Refractive index of the active region of the sensors are changed and at each step the output is simulated, and finally the normalized output is plotted as a function of the superstrate refractive index.

Figures 5.3 and 5.4 depict MZI sensor output normalized to input as a function of superstrate refractive index for MZ1 and MZ2 interferometers (see Figure 5.1). It can be seen that the sensitivity of the sensor increases with increasing the pathlength difference, Δl, or the window length, l. One can notice that symmetric design is more sensitive than the nonsymmetric design for devices of comparable length.

Figure 5.5 compares the sensitivity of the symmetric sensors with buried, MZ3, and ridge type, MZ1, refractive index profiles in the active region. Evidently, the device with ridge type refractive index profile is more sensitive than a similar one with buried

type. A symmetric sensor having a buried type profile with a window length of 5 mm exhibits a similar sensitivity to a symmetric sensor having a ridge type profile with a 3 mm long window. L does not appear to have an important role in the device sensitivity.

Figure 5.6 compares the sensitivity of two symmetric sensors having directional couplers instead of Y-junctions (sensor MZ4 in Fig.5.1). As expected, the sensor with the longer window exhibits higher sensitivity. Sensors with Y-junction exhibit the same sensitivity as the sensors with directional couplers (see Figures 5.3 and 5.6) (Malek-Tabrizi et al., 1996).

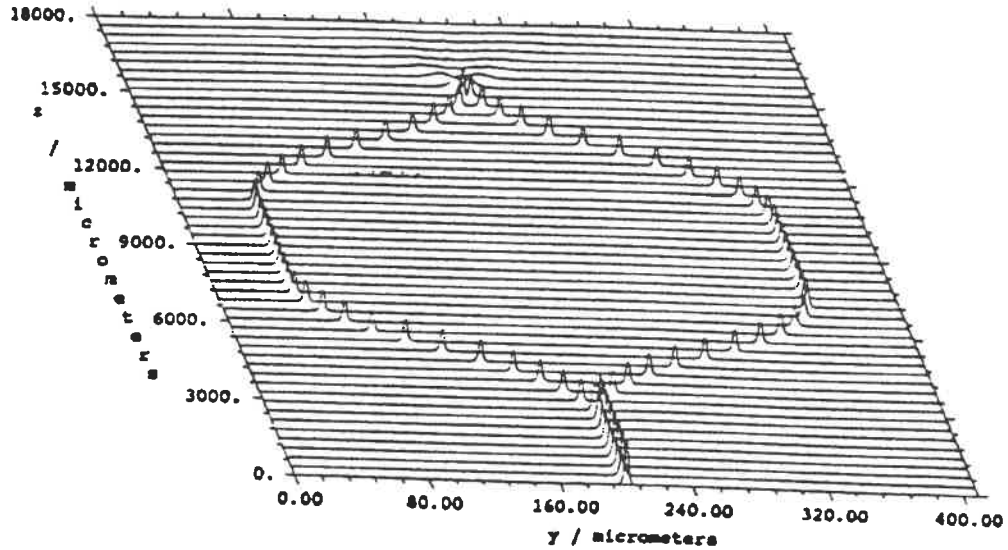

Figure 5.2.a. FD-BPM simulation of power in the Mach-Zehnder interferometer MZ1 (see Figure 5.1) with $\Delta\Phi=180°$ (from Malek-Tabrizi et al., 1996).

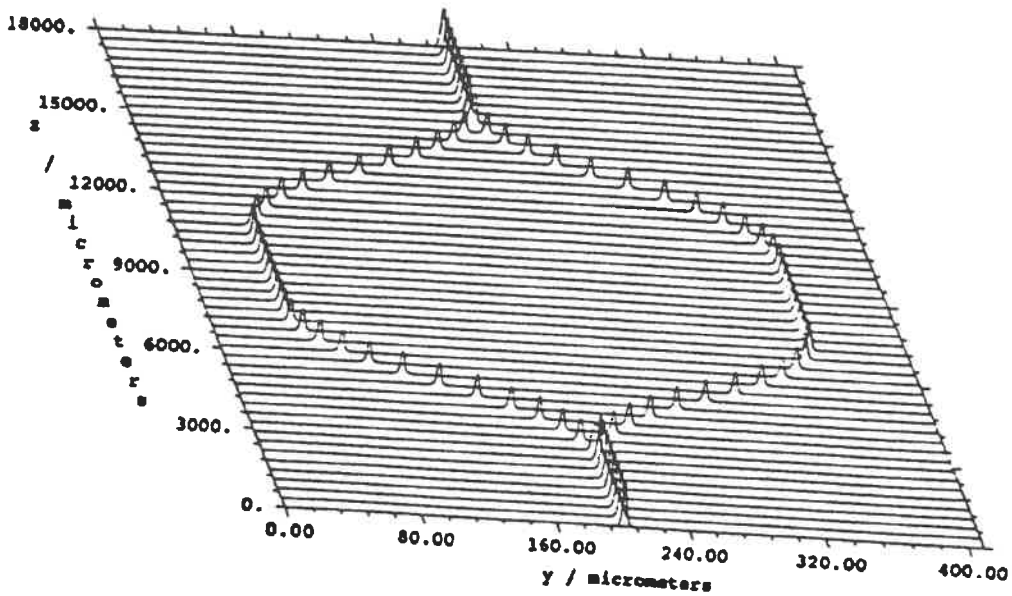

Figure 5.2.b. FD-BPM simulation of power in the Mach-Zehnder interferometer MZ1 (see Figure 5.1) $\Delta\Phi=0°$ (from Malek-Tabrizi et al., 1996).

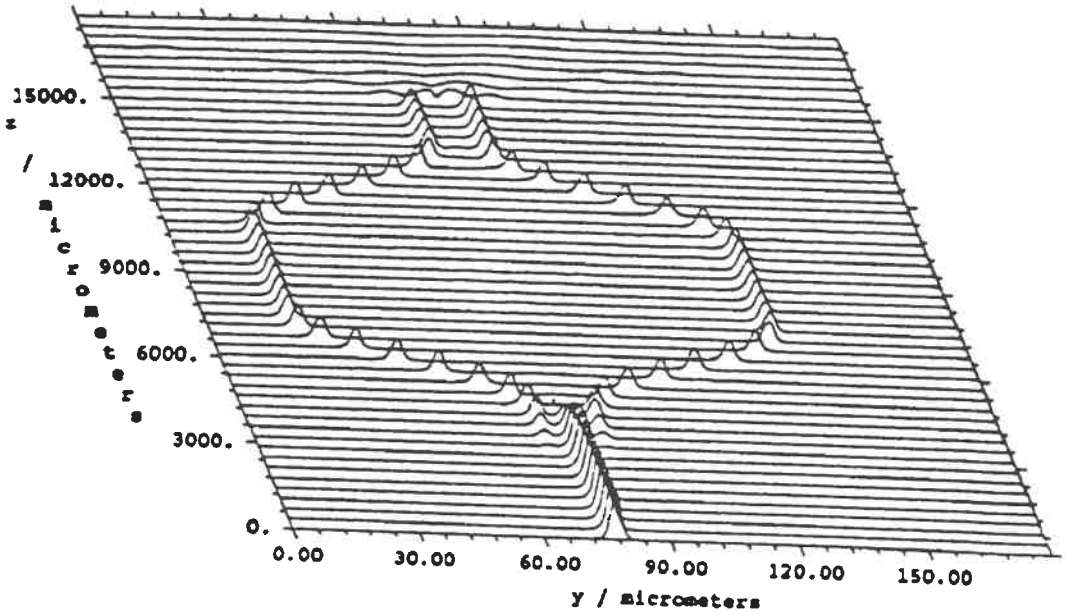

Figure 5.2.c. FD-BPM simulation of power in the Mach-Zehnder interferometer MZ4 (see Figure 5.1) with $\Delta\Phi=180°$ (from Malek-Tabrizi et al., 1996).

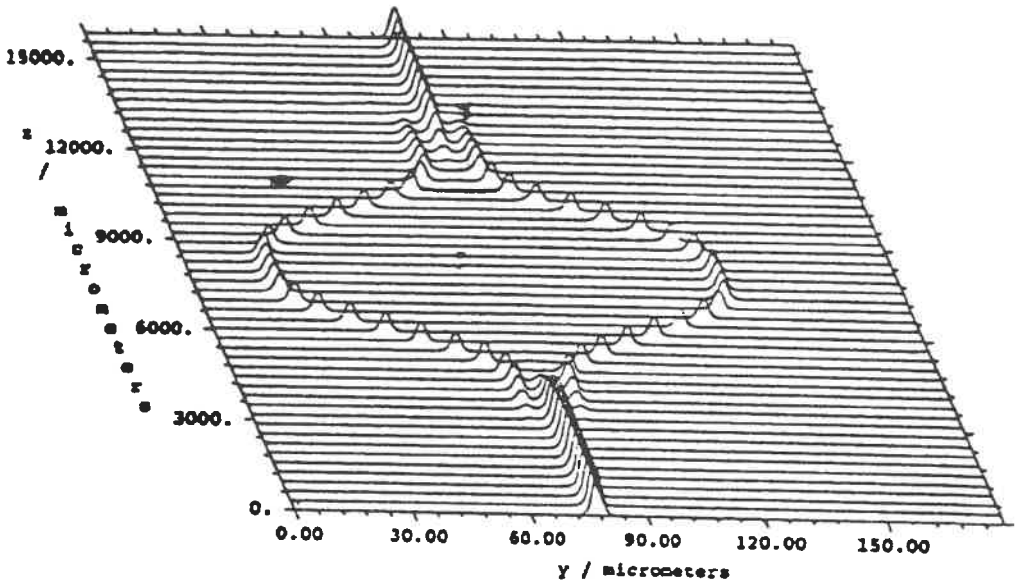

Figure 5.2.d. FD-BPM simulation of power in the Mach-Zehnder interferometer MZ4 (see Figure 5.1) with $\Delta\Phi=0°$ (from Malek-Tabrizi et al., 1996).

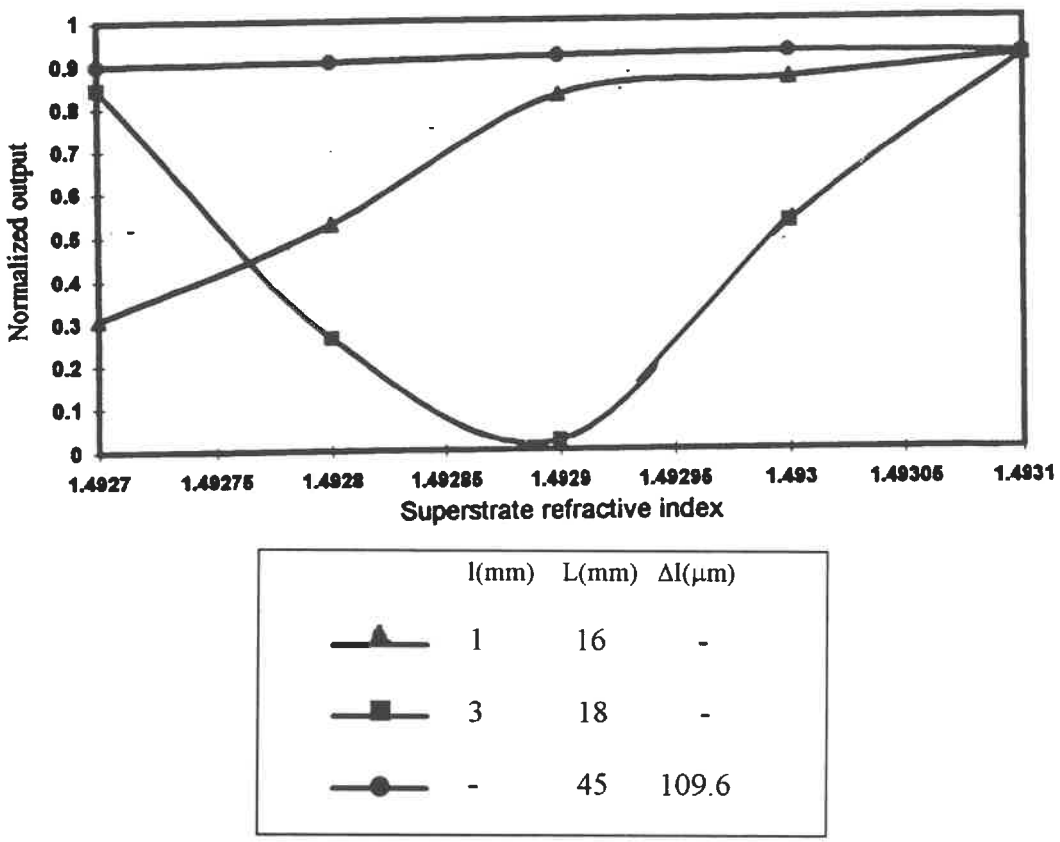

Figure 5.3. Mach-Zehnder interferometer sensor output intensity as a function of superstrate refractive index for symmetric MZ1 and nonsymmetric MZ2 interferometers (see Figure 5.1). l = window opening length for symmetric interferometer, Δl = path-length difference for nonsymmetric interferometer, L = device length (from Malek-Tabrizi et al., 1996).

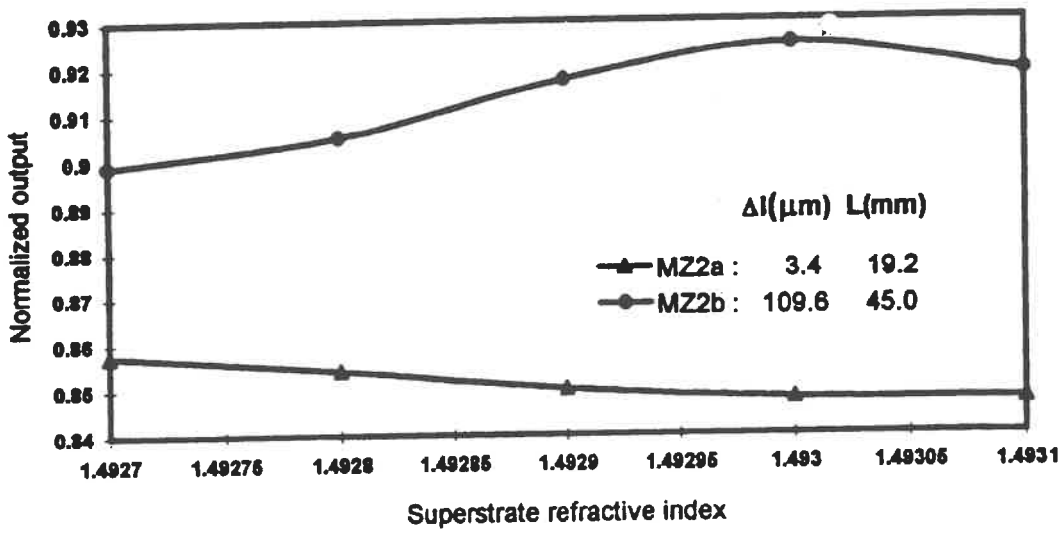

Figure 5.4. Mach-Zehnder interferometer sensor output intensity as a function of the superstrate refractive index for nonsymmetric MZ2 interferometer (see figure 5.1). Δl = path-length difference, L = device length (from Malek-Tabrizi et al., 1996).

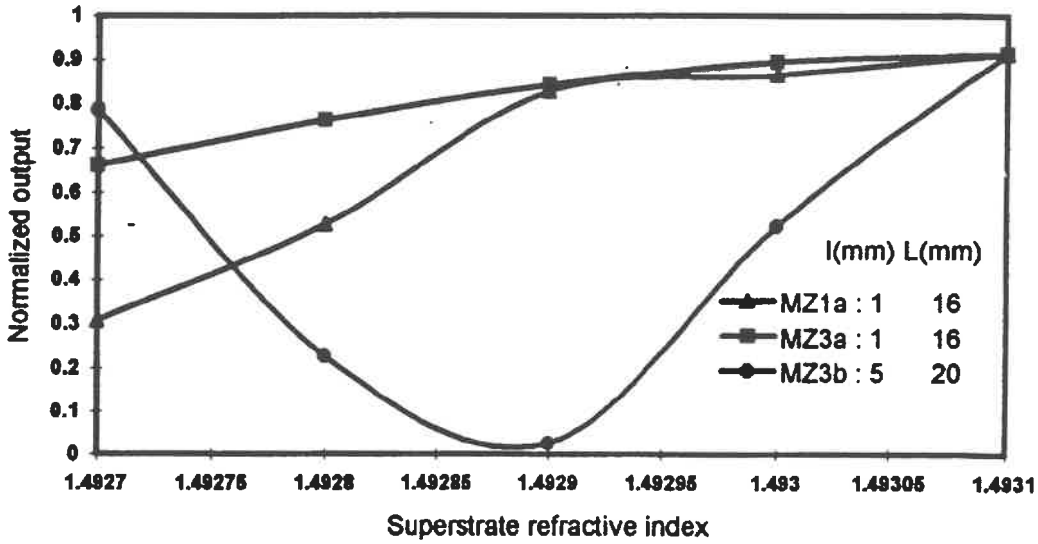

Figure 5.5. Mach-Zehnder interferometer sensor output intensity as a function of superstrate refractive index for ridge waveguide MZ1 and buried waveguide MZ3 symmetric interferometers (see figure 5.1). l = window opening length, L = device length (from Malek-Tabrizi et al., 1996).

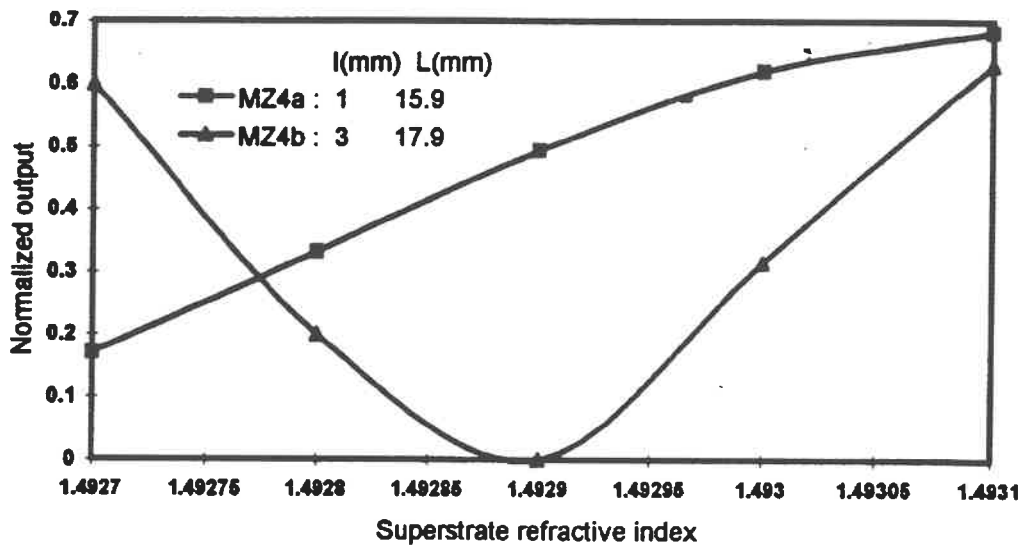

Figure 5.6. Mach-Zehnder interferometer output intensity as a function of the superstrate refractive index for symmetric MZ4 interferometer (see figure 5.1). l = window opening length, L = device length (from Malek-Tabrizi et al., 1996).

CHAPTER 6

NONSYMMETRIC MACH-ZEHNDER INTERFEROMETER

In Chapter 5 we concluded that the symmetric MZI is more sensitive than the nonsymmetric MZI. For further considerations, however, we chose to fabricate the nonsymmetric MZI because of its simplicity compared to the symmetric MZI which is very complex to fabricate and which has inherent absorption and thermal instability due to the existence of the window opening only in one arm of the sensor (Helmers et al., 1996). In the following, the design rules are explained and the fabrication steps are outlined. The experimental results from testing of the nonsymmetric Mach-Zehnder interferometer sensor are presented and discussed.

6.1. DESIGN

The first factor to consider in the design of the device is the profile design. The index profile chosen for the device should allow single mode operation of the device while having minimum coupling loss with a single mode fiber. Taking all of these aspects into account a mask opening of W = 2 μm was chosen (see Figure 6.1). The sensor is designed for the refractive index of the cladding ranging from 1.34 to 1.44 which could be easily obtained by solutions of sugar in water with different concentrations (Figure 6.4).

Potassium ion-exchange was chosen because this process provides, for the time being, substantially lower losses. Ion exchange was performed for 2 hours to obtain single-mode waveguides according to the procedure described in section 3.1.3. The profile calculation was performed for TE and TM polarizations whose index change in BK7 glass was found to be 0.008 and 0.011, respectively, (see Figure 6.2).

We know from Chapter 5 that larger path length difference between two arms of a nonsymmetric MZI makes it more sensitive. However, simple geometry tells us that larger path length difference means longer device, which is undesirable.

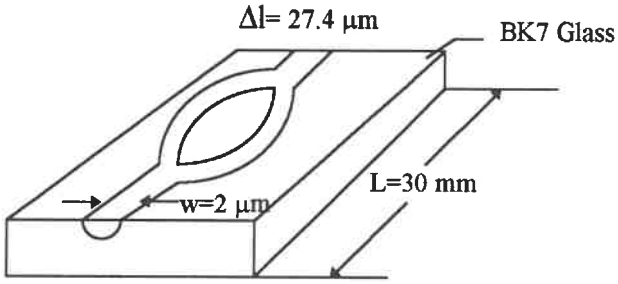

Figure 6.1. Mask layout and parameters for the Mach-Zehnder sensors.

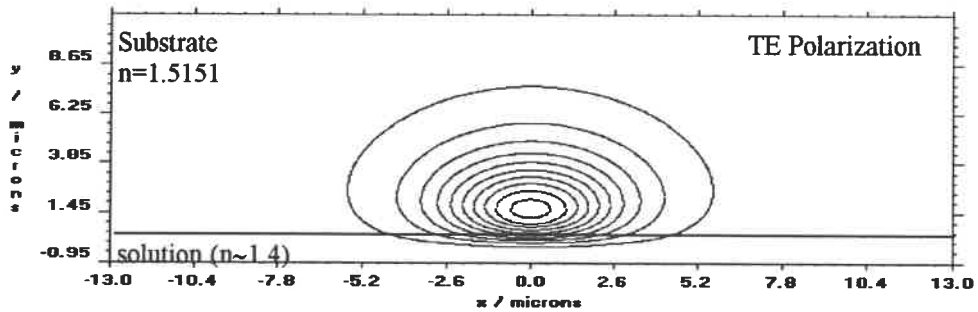

Figure 6.2. Mode profile of the active region of the device calculated for the potassium ion-exchange for 2 hours.

6.2. TESTING

The device was tested using the setup shown in Figure 6.3. Solutions of sugar and water with different concentrations were prepared as a model analyte. The refractive indices of the solutions were measured using a refractometer. A drop of each solution was placed on the MZI sensor and output was measured.

Different solutions of sugar in water were prepared which resulted in different refractive index values of the liquid measured by a refractometer (see Figure 6.4).

Figure 6.5 shows the measured and calculated output as a function of the solution refractive index. Each time the solution was placed on the device, the coupling was optimized and the measurement was performed. The next solution was applied after cleaning the device thoroughly with water and drying it. Figure 6.5 shows that the BPM simulation of the device agrees well with the experimental measurements obtained with the same device.

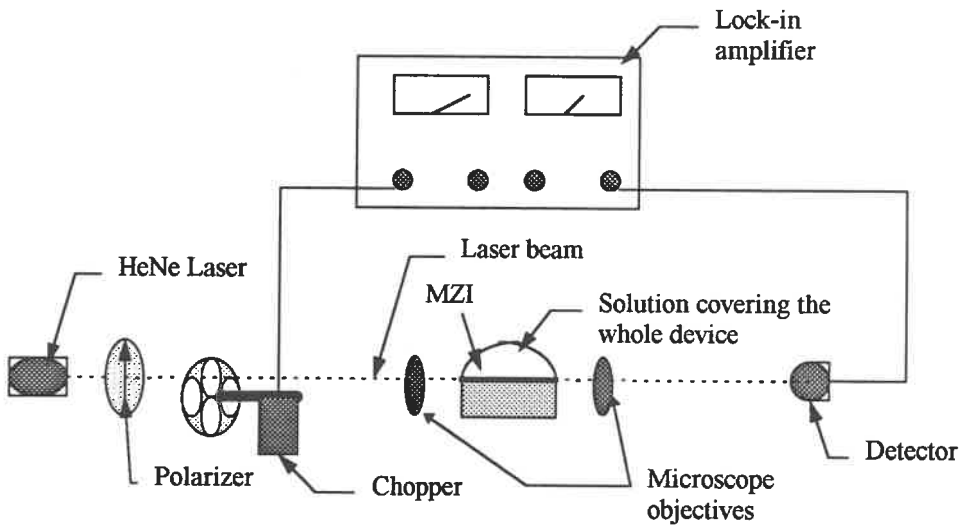

Figure 6.3. Setup for testing the prototype nonsymmetric MZI sensor.

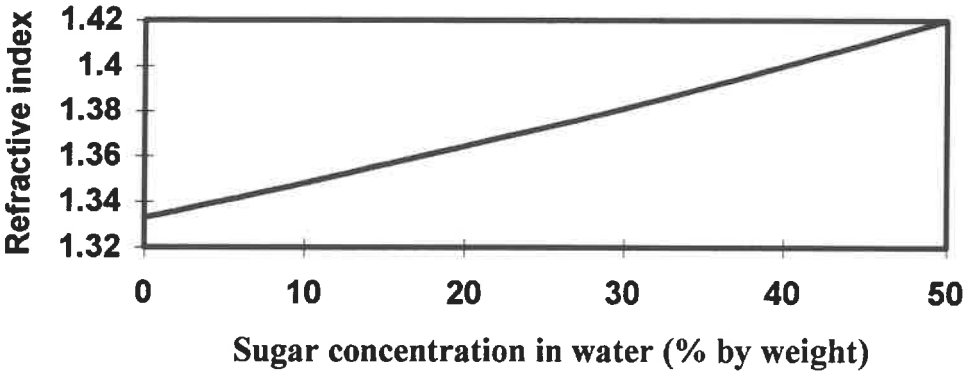

Figure 6.4. Refractive index of the analyte solution as a function of its concentration obtaied by refractometer at T=20°C and white light.

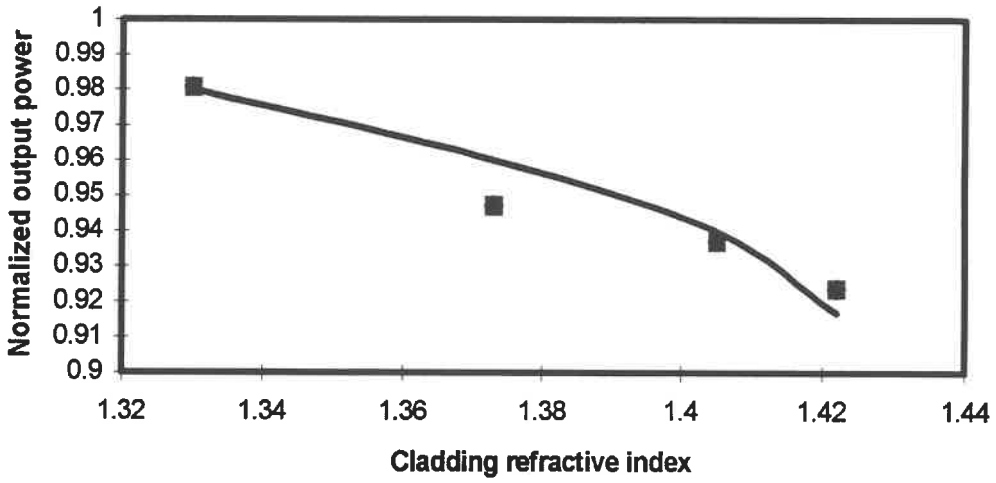

Figure 6.5. Normalized output power of a prototype nonsymmetric MZI vs. cladding refractive index: experimental data (■) compared with the FD-BPM simulation (solid line).

CHAPTER 7

CONCLUSIONS

In the present work ion exchanged and plasma deposited waveguides were fabricated by the methods described in Chapter 4, namely by PIE and PECVD. The channel ion exchanged waveguides were found to have Δn (refractive index change due to ion exchange) values (0.0081 ± 0.0001 for TE and 0.0110 ± 0.0001 for TM) equal to the one for slab ion exchanged waveguides, but their diffusion depth was smaller than that of slab waveguides. The diffusion depth decreased with the decreasing mask width. The refractive index dispersion curve for the plasma deposited films was determined using the reflection simulation method. Propagation loss for the plasma deposited waveguides was found to be from 5.0 to 7.6 dB/cm for different samples. These losses may be reduced by heating the substrate up to several hundred degrees Celsius during deposition, however, this creates inconvenience and increases production cost.

FD-BPM simulation results show that the symmetric Mach-Zehnder sensor is more sensitive than the non-symmetric Mach-Zehnder sensor with comparable device length. Increasing the window opening in the symmetric sensor and the path-length difference in the non-symmetric sensor enhances the sensitivity of the sensor. Sensors with the ridge waveguides in the active region have a higher sensitivity than the sensors with the buried waveguides: This can be explained in terms of the larger interaction area

with the analyte for the sensors with ridge waveguides in their active region. Mach-Zehnder interferometers with couplers demonstrate the same characteristics as the ones with Y-junctions.

K^+-exchange process was selected to produce the sensor because the losses in the PECVD waveguides are still too high for making a practical device. Considering the fabrication point of view, the non-symmetric MZI is simpler to prepare than the symmetric one since it involves only one level of masking in the photolithography.

Using the waveguide characteristics found for the ion exchange in BK7 substrate, a non-symmetric MZI was designed and fabricated. Testing of the sensor was performed by direct end launching of polarized HeNe laser beam into the device. During this procedure the whole sensor was covered with a model solution of sugar and water with a known concentration, and the output was recorded using a silicon photodetector. This process was repeated for several different concentrations of the solution. The data obtained show a very good agreement with the FD-BPM simulation of the same device and analyte. The "calibration" curve of the sensor shows that its sensitivity increases as we increase the refractive index of the solution. This is due to the fact that the evanescent tail of the mode is more expanding.

In conclusion, several aspects should be considered for future work; this involves: (i) decreasing the loss in the PECVD waveguides, (ii) fabrication of gas sensors by employing gas-sensitive polymers as the sensor's cladding, (iii) fabrication and testing of a prototype symmetric sensor, and (iv) testing other fabrication techniques such as sol-gel UV-imprinting.

REFERENCES

ALBERT, J., YIP, G.L. (1987). Stress induced index change for K^+-Na^+ ion exchange in glass. Elec. Letters, 23, 737-742.

BEARZOTTI, A., CALIENDO, C., VERONA, E., D'AMICO, A. (1992). Integrated optic sensor for the detection of H_2 concentration. Sensors and Actuators B, 7, 685-688.

BLAIN, S., KLEMBERG-SAPIEHA, J.E., WERTHEIMER, M.R., GUJRATHI, S.C. (1989). Silicon oxynitride from microwave plasma: fabrication and characterization. Can. J. Phys., 67, 190-194.

CHAPMAN, B. (1980). Glow discharge processes. Wiley-Interscience, New York, USA.

CHUNG, Y. and DAGLI, N. (1990 Aug.). An assessment of finite difference beam propagation method. IEEE J. of Quantum Elec, 26, 1335-1339.

ECKERTOVA, L. (1986). Physics of thin films. Plenum Press, New York, USA.

FABRICIUS, N., GAUGLITZ, G. and INGENHOFF, J. (1992). A gas sensor based on an integrated optical Mach-Zehnder interferometer. Sensors and Actuators B, 7, 672-676.

FISCHER K. and MÜLLER, J. (1992). Sensor application of SiON integrated optical waveguides on silicon. Sensors and Actuators B, 9, 209-213.

HELLESO, O.G., BENECH, P. and RIMET, R. (1995). Interferometric displacement sensormade by integrated optics on glass. Sensors and Actuators A, 46, 478-481.

HELMERS, H., GRECO, P., RUSTAD, R., KHERRAT, R., BOUVIER, G. AND BENECH, P. (1996 Feb.). Performance of a compact, hybrid optical evanescent-wave sensor for chemical and biological applications. Applied Optics, 35, 676-680.

JOHNSON, L.M. and LEONBERGER, F.J. (1982 Jul.). Integrated optical temperature sensor. Appl. Phys. Lett, 41, 134-136.

KAPSER, K., WAGNER, C., DEIMEL, P.P. (1991 Dec.). Rapid deposition od high-quality silicon-oxynitride waveguides. IEEE Transactions Photonics Technology Letters, 3, 1096-1098.

LAM, D.K.W. (1984 Aug.). Low temperature plasma chemical vapor deposition of silicon oxynitride thin-film waveguides. Applied Optics,.23, 2744-2746.

MALEK-TABRIZI, A., NAJAFI, S.I., MARTINU, L. (1996 Feb.). Glass integrated optics symmetric and non-symmetric Mach-Zehnder interferometer sensors. Conference on glass integrated optics and optical fiber devices, SPIE Photonics West '96, San Jose, USA.

MANOS, D.M., FLAMM, D.L. (1989). Plasma etching - An introduction. Academic Press, Boston, MA, USA.

MARTINU, L., KLEMBERG-SAPIEHA, J.E., and WERTHEIMER, M.R. (1989). Dual Microwave/ Radiofrequency plasma deposition of dielectric thin films. Applied Physics Letters, 54, 2645-2650.

MARTINU, L., KLEMBERG-SAPIEHA, J.E., KUTTEL, O.M., RAVEH, A., and WERTHEIMER, M.R. (1994). Critical ion energy and ion fluxin the Growth of films by PECVD. J. Vac. Sci. Technology A, 12, 1360-1368.

MARTINU, L. (1996). Low pressure plasma processing for optoelectronics applications. Conference on glass integrated optics and optical fiber devices, SPIE Photonics West '96, San Jose, USA.

MORT, J. and JANSEN, F. (1986). Plasma deposited thin films. CRC Press, Boca Raton, FL, USA.

NAJAFI, S.I. (1992). Introduction to glass integrated optics. Artech House, Boston, USA.

NISHIHARA, H., HARUNA, M., SUHARA, T. (1989). Optical Integrated Circuits. McGraw-Hill, New York, USA.

OHKAWA, M., IZUTSU, M. and SUETA, T. (1989 Dec.). Integrated optic pressure sensor on silicon substrate. Applied optics, .28, 5153-5157.

PACE, P.E., FOSTER, C.C. (1994). Beam propagation analysis of a parallel configuration of Mach-Zehnder interferometer. Optical Engineering, 33, 2911-2921.

POITRAS,D., LEROUX, P., KLEMBERG-SAPIEHA, J.E., GUJRATHI, S.C., MARTINU, L. (1996). Characterization of Homogeneous and Inhomogeneous Si-based Optical Coatings Deposited in Dual-Frequency Plasma. Optical Engineering, in press.

ROSSNAGEL, S.M., CUOMO, J.J., WESTWOOD, W.D. (1990). Handbook of plasma processing technology. Noyes Publications, Park Ridge, NJ, USA.

SMITH, D.L. (1990). Mat. Res. Soc. Symp. Proc., 69, 165-160.

SNYDER, W., LOVE, J.D. (1983). Optical waveguide theory. Chapman and Hall, New York, USA.

SRIRAM, S., PARTLOW, W.D., LIU, C.S. (1983 Dec.). Low-loss optical waveguides using plasma-deposited silicon nitride. Applied Optics, 22, 3664-3665.

TABASKY, M., BULAT, E.S., TWEED, B. AND HERRICK, C. (1994). Investigation of thick, low temperature plasma deposited silica films for waveguide fabrication. J. Vac. Sci. Technol. A, 12, 1244-1250.

TATIAN, B. (1984 Dec.). Fitting refractive-index data with the Sellmeier dispersion formula. Applied Optics, 23, 4477-4485.

TERVONEN, A. (1990). Optical waveguides by ion exchange in glass: fabrication processes for integrated optics application. Dissertation no. 28, University of Helsinki, Finland.

TIEN, P.K., SMOLINSKY, G., AND MARTIN, R.J. (1972). Thin organosilicon films for integrated optics. Applied Optics, 11, 637-639.

UDD, E. (1991). Fiber optics sensors. John Wiley & Sons, Inc., New York, USA.

WAGNER, C., FRANKENBERGER, J. and DEIMEL, P.P. (1993 Oct.). Optical pressure sensor based on a Mach-Zehnder integrated with a lateral a-Si:H p-i-n photodiode", IEEE photonics technology letters, 5, 1257-1259.

WANG, W.J., HONKANEN, S. and NAJAFI, S.I. (1993). Loss characteristics of potassium and silver double-ion-exchanged waveguides. J. Appl. Phys, 74, 1529-1533.

ÉCOLE POLYTECHNIQUE DE MONTRÉAL
3 9334 00171628 9